Accepted Manuscript

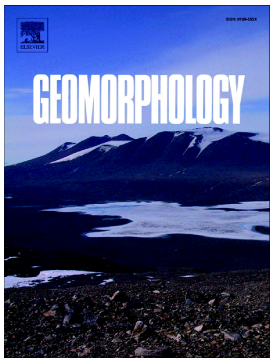

Potential of airborne LiDAR data analysis to detect subtle landforms of slope failure: Portainé, Central Pyrenees

María Ortuño, Marta Guinau, Jaume Calvet, Glòria Furdada, Jaume Bordonau, Antonio Ruiz, Miquel Camafort

PII: S0169-555X(17)30292-1
DOI: doi: 10.1016/j.geomorph.2017.07.015
Reference: GEOMOR 6078

To appear in: *Geomorphology*

Received date: 12 February 2016
Revised date: 5 July 2017
Accepted date: 15 July 2017

Please cite this article as: María Ortuño, Marta Guinau, Jaume Calvet, Glòria Furdada, Jaume Bordonau, Antonio Ruiz, Miquel Camafort , Potential of airborne LiDAR data analysis to detect subtle landforms of slope failure: Portainé, Central Pyrenees, *Geomorphology* (2017), doi: 10.1016/j.geomorph.2017.07.015

Potential of airborne LiDAR data analysis to detect subtle landforms of slope failure: Portainé, Central Pyrenees

María Ortuño[a,*], Marta Guinau[a], Jaume Calvet[a], Glòria Furdada[a], Jaume Bordonau[a], Antonio Ruiz[b], Miquel Camafort[c]

[a] RISKNAT group, Geomodels Institute, Departament de Dinàmica de la Terra i de l'Oceà, Facultat de Ciències de la Terra, Universitat de Barcelona (UB), Martí i Franquès s/n, 08028 Barcelona, Spain

[b] ICGC, Institut Cartogràfic i Geològic de Catalunya, Parc de Montjuïc, 08038 Barcelona, Spain

[c] Centre Mediterrani d'Investigacions Marines i Ambientals-CSIC, Psg. Marítim de la Barceloneta, 37-49, 08003 Barcelona, Spain

***** Corresponding author. Tel.: +34-93-402-1378; Fax.; +34-93-402-1340.

E-mail: maria.ortuno@ub.edu (M.Ortuño)

Abstract: Slope failures have been traditionally detected by field inspection and aerial-photo interpretation. These approaches are generally insufficient to identify subtle landforms, especially those generated during the early stages of failures, and particularly where the site is located in forested and remote terrains. We present the identification and characterization of several large and medium size slope failures previously undetected within the Orri massif, Central Pyrenees. Around 130 scarps were interpreted as being part of Rock Slope Failures (RSFs), while other smaller and

more superficial failures were interpreted as complex movements combining colluvium slow flow / slope creep and RSFs. Except for one of them, these slope failures had not been previously detected, albeit they extend across a 15% of the studied region. The failures were identified through the analysis of a high-resolution (1 m) LIDAR-derived bare earth Digital Elevation Model (DEM). Most of the scarps are undetectable either by fieldwork, photo interpretation or 5 m resolution topography analysis owing to their small heights (0.5 to 2 m) and their location within forest areas. In many cases, these landforms are not evident in the field due to the presence of other minor irregularities in the slope and the lack of open views due to the forest. 2D and 3D visualization of hillshade maps with different sun azimuths provided an overall picture of the scarp assemblage and permitted a more complete analysis of the geometry of the scarps with respect to the slope and the structural fabric. The sharpness of some of the landforms suggests ongoing activity, which should be explored in future detailed studies in order to assess potential hazards affecting the Portainé ski resort. Our results reveal that close analysis of the 1 m LIDAR-derived DEM can significantly help to detect early-stage slope deformations in high mountain regions, and that expert judgment of the DEM is essential when dealing with subtle landforms. The incorporation of this approach in regional mapping represents a great advance in completing the catalogue of slope failures and will eventually contribute to a better understanding of the spatial factors controlling them.

Keywords: Bare-earth topography; Landslide mapping; Slope deformation; Arrested RSF

1. Introduction

1.1. Slope failures detection from LiDAR derived DEMs

The analysis of high resolution Digital Elevation Models (DEMs) derived from Light Detection and Ranging (LiDAR) data has opened a new era in the study of slope failures. Development and

subsequent evolution of airborne LiDAR have enabled us to obtain 3D topographic data over large areas with sub-metric spatial resolution (Slatton et al., 2007; Heritage and Large, 2009). The amount of papers showing the benefits of using LiDAR derived DEMs for the understanding of slope processes has rapidly increased during the last decade as indicated by Derron and Jaboyedoff (2010), Jaboyedoff et al. (2010), Guzzetti et al. (2012), Roering et al. (2013) and Tarolli (2014). This successful application enables the detection of landforms otherwise indiscernible with conventional methods for a number of reasons: 1) it furnishes an overview of the landforms within a wide area, which is a direct advantage over field mapping; 2) it permits the analysis of the bare earth surface below the canopy of forested terrains, overcoming some of the handicaps posed by the analysis of stereo pairs and satellite images (Ardizzone et al., 2007; Van Den Eeckhaut et al., 2007, 2011; Guzzetti et al., 2012; Roering et al., 2013; Konsoer and Kite, 2014); and 3) high resolution DEMs obtained from LiDAR data allow us to detect small changes in slope that would be difficult to detect by photogrammetry (Haugerud et al., 2003; Schulz, 2004; Van Den Eeckhaut et al., 2007; Guzzetti et al., 2012; Lin et al., 2013; Razak, 2014).

The lack of systematic studies of slope failures in mountainous regions worldwide is one of the current problems in assessing the risk of mass movements and evaluating the main factors controlling their spatial distribution. Recent studies have focused on the development of computerized methodologies for the automatic or semi-automatic detection of different types of mass movements or analysis of susceptibility and hazards (McKean and Roering, 2004; Glenn et al., 2006; Booth et al., 2009; Kasai et al., 2009; Van Den Eeckhaut et al., 2012; Razak, 2014; Mora et al., 2015; Palenzuela et al., 2015). Most methodologies are focused on detecting unstable zones from local surface roughness. Although these methods enable us to find out the main features of the slope failure (main scarps, reverse slopes, and landslide foot-convexity), other minor features (usually less than 2–3 m high) such as minor scarps, cracks, and small concavities or convexities, remain undetected (Glenn et al., 2006; Tarolli et al., 2012; Van Den Eeckhaut et al., 2012).

Accordingly, when automatic detection methods are used, most slope failures composed of multiple and complex features with different geomorphological characteristics are commonly simplified into a few types of landforms.

The study of subdued large-scale slope failures could benefit from geomorphologic expert analysis of high resolution LiDAR-derived DEMs to determine the extent of the slope failures and to understand the processes involved, especially in areas where they have not been detected before.

In this paper we present the geomorphological study of a small pilot area (60 km^2) within a sector of the Pyrenees lacking a regional inventory map of slope failures. As highlighted by Van Den Eeckhaut and Hervás (2012), the official landslide databases of Catalonia (NE Spain) have a low completeness (<25%) that hampers the landslide risk assessment. The studied area is affected by subdued large (> 0.25 km^2) and complex slope failures. These slope failures had not been previously detected by conventional mapping methods due to 1) their weak topographic and morphologic expression related to their relatively small height, and 2) their location in forested areas. The methodological approach includes the analysis of 2D and 3D views of shaded-relief and contour maps from a 1 m LiDAR derived DEM, of a 5 m DEM derived from photogrammetry, and their comparison with the available orthophotos, stereo pairs and ground tests.

1.2. Identification and classification of subdued large slope failures.

The failure mechanisms, the control and trigger factors and the regional distribution of large slope failures in mountain regions need to be better studied (Crosta and Clague, 2006). To properly advance these fields, detailed mapping of slope failure landforms is required from their early stages up to the more easily recognizable advanced stages. Detailed mapping of slope failures will provide improved information on the relationships between slope failures and their local or regional

controlling factors such as lithology, geological structures, and stress changes due to glacial retreat or different seismic amplification effects.

The use of LiDAR technology in the recognition of subdued slope failures in populated regions should lead to a noticeable improvement in the forecasting of catastrophic failures since they might develop incipient landforms before their occurrence. Unlike other remote techniques such as satellite imagery and aerial photointerpretation, the LiDAR approach allows the detailed mapping of discrete landforms in forested areas (for instance, scarps less than 2 m high were detected by Tarolli et al., 2012), providing also an overall image of the landform assemblage of the whole slope and a better understanding of progressive slope failures (Petley et al., 2005).

Early-stage features of mass movements are often not distinctive enough for classification and mapping slope failure types. However, some types of slope failures will never evolve to any other types since the early stage. In this paper, we try to infer the type of slope deformation affecting the Portainé area, and classify the types of slope failures (e.g., Varnes, 1978; Hutchinson 1988; Evans and Clague, 1996; Hungr et al., 2014). We adopted the umbrella terms "Rock Slope Failures" (RSFs) and "Superficial Failures", as proposed by Jarman (2006). An RSF refers to gravitational downslope movements affecting a significant bedrock mass larger than 0.01 km^2, leading to the loss of its structural integrity. This term does not imply any constrains neither in the amount of distance travelled nor in the amount of dislocation involved. In order to follow a pragmatic and convenient approach, we have used the subtypes of RSFs contemplated by Jarman et al. (2014) for the Eastern Pyrenees, which are inspired by the classification of Evans and Clague (1996), emphasizing complete vs. arrested failures and the stages in between these end members. These subtypes are: 1) cataclasmic RSF, as complete failures in which the affected mass has traveled to the slope toe losing its structural integrity (called sub-cataclasmic if the mass is still largely on the slope); 2) arrested RSF that has travelled a relatively short distance, retaining most of the original structure; and 3) slope deformation, reserved to the RSF that has remain "*quasi in situ*" and typically presents

antislope scarps and double ridges. This subtype of RSF has been classically known as "sackung" when also displaying a bulge in the middle-lower part of the slope.

The slow gravitational movements involving thick portions of rock under the surface have been broadly referred to as "deep-seated gravitational slope deformations" in the literature (DGSD or DSGSD; e.g., Crosta, 1996; Agliardi et al., 2001; Korup, 2006; Bachmann et al., 2009; Hippolyte et al., 2012), as it was recommended by Dramis and Sorriso-Valvo (1994). Although no reference value is found as broadly accepted to fix the depth of deformation of the DSGD, most cases refer to more than 100-150 m depths within the slope (e.g., Crosta, 1996; Hutchinson, 1995). We found more appropriate to avoid these terms due to the lack of sufficient data confirming the depth of the failure zone within the mountain ridge. Most of the slope failures classified in the literature as DSGD fit well with the arrested RSF and Slope Deformation sub-types of Jarman (2006), which are considered here more appropriate terms because they are not limited to failures reaching deep areas down within the mountain ridge.

1.3. Slope Deformations within the Pyrenees.

In the Pyrenees, little work has been done to analyze the regional distribution of slope deformations. At least 32 RSFs corresponding to the subtypes of subcataclasmic and arrested failures have been mapped and documented in the Central and Eastern Pyrenees: twelve of these RSFs are located within the Central Pyrenees; two in the Boí-Taüll valleys (Soeters and Rengers, 1983; Ortuño, 2008); one in the Hurno range, southwest from Vielha (Bordonau and Vilaplana, 1986, Ortuño, 2008); two in the Ésera drainage area, north of Benasque (Gutiérrez-Santolalla et al., 2005; Gutiérrez et al., 2008; Ortuño, 2008); one in the Encampadana ridge in Andorra (Hürlimann et al., 2006); three more cases within the Maladeta-Aigüestortes massif (Ortuño, 2008); and three related to lateral spreading on evaporitic formations within the Peracalç range (Gutiérrez et al., 2012). Jarman et al. (2014) identified 20 large rock slope failures in the Central-Eastern Pyrenees

(six in the Central sector and 14 in the Eastern sector) by remote sensing, field inspection and literature review. All of these failures refer to relatively large scarps and landforms detectable by conventional mapping methods. Reference dimension values of the most prominent scarps are 30 to 90 m in height (Gutiérrez-Santolalla et al., 2005; Gutiérrez et al., 2008; Jarman et al., 2014). Jarman et al. (2014) highlight the need of further refined mapping to better understand the slope failure distribution. Their provisional conclusions suggest that the low frequency of large slope failures in the Eastern Pyrenees could be related to the attenuated glacial erosion with respect to other European regions.

In the report of the *Institut Cartogràfic i Geològic de Catalunya* (ICGC, 2013) for the Portainé study area, where LiDAR DEMs were used, some scarps were detected by the authors of the present paper to pinpoint the presence of large-scale slope failures previously undetected. The present paper has further developed this preliminary study.

2. Geological and geomorphological setting.

The Portainé area is located in the southern central Pyrenees (**Figs. 1** and **2**). The highest peak is Torreta de l'Orri (2437 m a.s.l.), and the village of Rialp beside the Noguera Pallaresa river is the lowest point at about 700 m a.s.l. The area is drained by the fluvial system of the Noguera Pallaresa River, a tributary of the Ebro River draining to the Mediterranean Sea. Springs are common in the area due to the snow cover and the thick soils. A ski resort occupies the center of the study area, and it is installed in the headwaters of the Ramiosa, Portainé and Reguerals catchments (**Fig. 2**).

Vegetation mostly consists of dense conifer forests (up to 2300 m a.s.l.) with some deciduous trees predominantly near the streams, and some bushes and herbaceous crops at medium altitudes; from 2100 m upwards there are pastures with some patches of rhododendron bushes (CREAF, 2009). Dense forest covers most of the slopes, smoothing and masking small-scale landforms.

2.1. Geological setting

The geological structure of the Pyrenees consists of a W-E oriented asymmetric double wedge formed during the Alpine orogeny as a result of the collision between the Iberian and European plates. In the southern wedge, three hinterland thrust sheets, Rialp, Orri and Nogueres from bottom to top, are identified (Muñoz, 1992; Beaumont et al., 2000). The studied area is located within the middle Orri sheet (**Fig. 1**), in an antiformal domain called the Orri dome (Schmidt, 1931; Poblet, 1991).

The bedrock consists of strongly folded and faulted Cambro-Ordovician metasedimentary rocks (shales and sandstones), locally covered by Quaternary deposits (Hartevelt, 1969; Poblet, 1991). The rock structure is dominated by the intersection of seven deformation phases that have generated multiple planar fabric features (tension fractures, axial plane cleavages, thrusts and faults, etc.). Those features show a variable orientation resulting in a complex set of structures. In the study area, the cleavage generated during the second folding phase is the most outstanding feature. It shows a WNW–ESE trend and a highly variable dip angle (10–67º) towards the north. This cleavage is affected by thrusting and shearing along SE–NW to E–W trending planes dipping between 10 and 55º towards the north. The youngest structural features in the area consist of N–S normal faults of variable dip (subhorizontal to 55º both towards the E and W) related to the collapse of the Orri dome. The thrusts and faults present in the area have associated breccias and fault gauges with a maximum decimetric thickness (Poblet, 1991).

2.2. Geomorphology

The main geomorphological features of the studied area are constituted by even, smooth mountain ridges corresponding to Neogene summit surface remnants, which separate fluvial valleys

where active fluvio-torrential and slope processes dominate. Also, small glacial cirques are encroached into the highest areas (**Figs. 2** and **3**).

The ridge extending from the north oriented watersheds of Caners and Ramiosa to the rounded top of Torreta de l'Orri (2437 m a.s.l.), with gentle slopes (<15º), corresponds to one of these summit surface remnants (Hartevelt, 1969, 1970) which are common in the Pyrenees (Boissevain, 1934; Zandvliet, 1960; Serrat et al. 1994; Babault et al., 2005; Gunnell et al., 2009; Jarman et al. 2014). They formed before the Pleistocene glaciations. Despite a general lack of dating, Ortuño et al. (2013) suggested that they formed before the Late Miocene because they are covered by Vallesian deposits (11.1–8.7 Ma) in the Prüedo area (Aran Valley), about 40 km northwest of the studied area.

The regional uplift of the Pyrenees during the Pliocene and Quaternary caused rapid incision of the valleys, dissecting the paleic relief. The post-orogenic fluvial drainage network of the southern flank of the Pyrenees is strongly controlled by the connection of the Ebro basin with the Mediterranean Sea during the late Miocene (e.g., García-Castellanos et al., 2003), which caused a sudden lowering of the base level and lead to the formation of deeply entrenched Quaternary valleys (Stange et al., 2014).

The main rivers draining the Pyrenees (such as the Noguera Pallaresa) show a N-S direction transverse to the main E-W alpine structures. In the study area, the drainage network is mainly determined by tectonic lineaments, both variscan (Zandvliet, 1960), and alpine. The Romadriu River, mostly structurally conditioned and the even smaller scale subparallel streams draining northwards, run incised on the Cambro-Ordovician rocks of the Orri dome unit (**Figs.** 1 and 2).

Pleistocene glaciations affected the entire Pyrenees although nearly all the present glacial deposits and landforms are attributed to the last glaciation in the Upper Pleistocene. The studied area is in a peripheral, essentially non-glacial sector, with the southernmost small glacial features in

the Noguera Pallaresa basin: four cirques with their floors at around 2000–2100 m a.s.l. Thus, the area is mostly located in the domain of the fluvial processes. The only north oriented cirque is affected by a large slide mapped by Hartevelt (1969, 1970). Rock glacier moraines, moraines and tills have been eroded and reworked by the installations of the Port-Ainé ski resort and by postglacial processes.

Those areas not occupied by glaciers during the Pleistocene were affected by intense periglacial processes, producing a large amount of debris feeding thick soils (>10 m) that regularized the north facing slopes of the studied area. Moreover, continued fluvial and torrential incision originated a high relief (500–1000 m) with narrow valleys and steep slopes ranging from 10–20^{o} between 1500–2000 m a.s.l. to 20-50^{o} below 1500 m a.s.l., where much destabilisation with rapid removal of small-scale RSFs can happen.

3. LiDAR data acquisition and processing.

Airborne LiDAR data in the Portainé area belong to the LiDARCat project that covers Catalonia (NE Spain). Data acquisition and post-processing were carried out by the *Institut Cartogràfic i Geològic de Catalunya* (ICGC), with a LiDAR system ALS50-II (Leica). LiDARCat is also part of the PNOA project that covers Spain with orthophotos and LiDAR DEMs (Ojeda, 2012).

3.1. Flight and system parameters

Flight and system parameters applied to the Portainé area (Table 1) were carefully defined because it is a mountainous region difficult to survey. In this steep area the flying height and other system parameters were set differently for each strip depending on the range of terrain elevations to be covered. Some strips had to be flown at two different flying heights to cover both the valleys and the peaks due to the high relief. Flight plans were designed with a minimum strips overlap of 50%. The resulting point density ranges between 0.8 to >2.86 points m^{-2}. The GPS frequency was 1 Hz

and the INS frequency 200 Hz. The 37 strips covering the Portainé area were obtained in 19 flight sessions, eight strips in 2009 and the rest in 2011.

The estimated precision of the point coordinates according to the system manufacturer is shown in Table 1. These values correspond to direct orientation and, in this case, the horizontal error is more than twice the vertical error. Making use of ground control and the sensor trajectory systematic errors were reduced with a least squares adjustment with TerraMatch (Burman, 2000).

3.2. Bare-earth DEMs production and derived maps

After applying the estimated corrections, the LiDAR point cloud was classified into ground and vegetation points with TerraScan (Terrasolid, 2016) following the TIN-iterative method (Axelsson, 2000). On steep terrain and with the presence of vegetation, the precision is reduced and classification errors are more frequent. Thus, the density of points classified as ground may be significantly lowered in those areas. Next, a manual editing of the classification was performed by trained operators, and a raster bare-earth DEM with 1 m grid step was produced from the classified ground-points by interpolating the TIN model with flat triangles.

From the bare-earth DEM, several shaded relief and topographic contour maps were obtained with ArcGIS Spatial Analyst by ESRI (ESRI, 2016). Computer generated shaded relief maps emphasize structures that are obliquely illuminated, but hide those that are aligned with the illumination direction, particularly when dealing with linear landforms (Smith and Clark, 2005; Devereux et al., 2008; Bennett et al., 2012). Thus, hillshade maps were created with a constant sun altitude of 45º and variable sun azimuths of 45°, 135°, 225° and 315°, in order to avoid azimuth-bias in the interpretation of landforms. The shaded-relief map providing the most significant linear structures was used to locate the identified features in **Figs. 3** to **6**. Moreover, topographic contour maps were generated with 10 and 2 m contour intervals and overlaid on the shaded-relief maps. These hillshade contour maps assisted in the morphological analysis both to locate topographic

profiles perpendicular to landforms and to calculate the dip of main and minor scarps. **Fig. 7** illustrates how some of the detected scarps are only distinguishable with a particular azimuth. These examples are commented below, in Section 4.

The 3D visualization of shaded-relief maps in ArcScene (ESRI, 2016) provides multiple perspectives of the landscape, allowing the identification of features not well seen in plan view / 2D. The use of different sun azimuths and the combination of 2D and 3D visualization of the LiDAR derived maps have become the most appropriate method in the study area, due to the multiple orientations of the landslide features. For instance, a rotational slide indiscernible in the planimetric view was identified by the 3D visualization of the hillshade with a 315º sun azimuth (**Fig. 8**, zone A3, Supplementary material 3, see **Fig. 3** for the location of zone A3).

The 1 and 5 m DEMs were compared, although the 1 m DEM was used as the main tool to detect several landslide features such as scarps, scars, cracks, reverse slopes and other related linear structures. The 5 m DEM was also interpreted but, as shown in **Figs. 4** to **6**, the 1 m DEM was more helpful in locating the landslide features.

4. Geomorphological analysis of the slope failures.

4. 1. Work-flow for mapping landforms of slope failure

Slope failures in the Portainé pilot study area were detected by the integrated analysis of the DEM in map and 3D views, stereo pairs (1:26,000 from 1956 and 1:30,000 from 1982) and orthophotos (1:5,000 from 2013). The selection of the stereo pairs of the studied zones in the 1956 flight is provided in the supplementary files. A systematic description of the slope failures was made referring to their geometry, orientation, appearance, size and slope dip. The visibility of these features in the different base layers was also analyzed (Table 2). Additionally, we have performed a "blind test" to get a more robust diagnosis of the visibility of the features mapped with

photointerpretation versus those mapped through the interpretation of the LiDAR shaded maps and 3D images. To do so, two geologists with experience mapping landslides in the Pyrenees (expert 1, more than 20 years of background) and in the Andes (expert 2, recently graduated with an MS degree in Geological Hazards) analyzed the stereo pairs (supplementary materials 1 and 2), and produced two landform maps only based on photointerpretation (supplementary materials 4 and 5). The presence, dimensions and appearance of a selected group of 33 scarps (numbered in **Figs. 3** to **10**) were checked during a 3-day-long survey. Ground-truth by direct inspection in the field confirmed that the selected scarps are real and have dimensions that fit well with those inferred from the analysis of the LiDAR DEM. However, many of these landforms, especially in zones A and C, are not evident in the field due to the presence of other minor irregularities in the slope and to the impossibility of having open views due to the forest. The scarps identified were grouped into three zones named A, B and C (**Figs. 3** to **6**). These zones share similar lithology and structure, but are affected by different types of slope failures probably resulting from local differences in the degree of weathering, relief and location with respect to the glacial and fluvial drainage network. For each zone, the basic geometrical characteristics were obtained through cross-sections, which provided maximum heights of the scarps (specified in the captions of **Figs. 4** to **6**) and helped to get a rough estimate of the geometry of the scarps at depth (**Fig. 11**). To build these sections, we obtained topographic profiles from the 1 m DEM. The profiles were oriented following the maximum slope (i.e. suspected direction of displacement). We then located the scarps along the profile according to their mapped traces and drew the hypothetical continuation in depth of these scarps. The proposed sections seem consistent with the observed landforms but are only based on detailed surface mapping of the traces. Thus, they should be considered as a first estimation. The in-depth geometries of some of the failure planes (marked with bold red lines in **Fig. 11**) correspond to the best fitting surface containing the trace of the scarp. These geometries are derived by: 1) extracting the XYZ coordinates (3D line) of the trace of the head scarps once projected on the 1 m

DEM (the 3D line is made of consecutive points separated by 1 m in the map); and 2) using the ArcGIS Spatial Analyst tool by ESRI (ESRI, 2016), which applies the "natural neighbor interpolation" proposed by Sibson (1981) to obtain the surface containing this 3D line points. This analysis was only applied to arc-shaped head scarps, for which the number of possible containing surfaces is more limited, compared to rectilinear scarps.

The interpretation of each assemblage of slope features in terms of slope failure typology was made according to 1) the geometry of the scarp assemblages and their position and orientation with respect to the slope, 2) the slope profile, 3) the lithology, 4) the relative orientation of the scarps and the bedrock structure, and 5) the location of the failure with respect to the main drainage network. The classification of the main landforms into different slope failures was done using the criteria discussed in Hungr et al. (2014) and the general classification proposed by Jarman et al. (2014).

4. 2. Zone A

Within Zone A, four areas affected by slope failures are identified affecting the slopes of the Portainé and Reguerals valleys (**Figs. 2** and **3**). The slope failures concentrate along the gentle (<10º) mountain ridges and along the upper valley sides (10–17º). The affected area lies in a fluvial valley almost fully covered by forest (**Fig. 4**).

4.2.1. Zones A1 and A2

These zones (**Fig. 3**) show three arcuate north-facing downslope scarps (A1) and three antislope scarps (A2). Failures at A1 are inferred from the presence of several minor downslope scarps parallel to a major head scarp which is composed of three segments: scarp #5 in **Fig. 9** (0.70 m measured in the field), scarp #3 in **Fig. 9**, with a larger height (15 m of cumulated offset at the central part of the trace as inferred from topographic profile, **Fig. 11**), and a more subdued scarp at the western part. The scarp lengths range between ~1 km and 100 m. These features are clearly

visible in the 1 m DEM, but not in the 5 m DEM (**Fig. 4**), where only the trend of the scarps #3 and #4 in **Fig. 9** is suspected by a change in roughness. Even in the 1 m LiDAR, only some azimuths of illumination permitted to track a maximum number of scarps. This zone is a good example of how it is important to use different hillshade models (with different illuminations) to complete the 2D mapping of the scarps (**Fig. 7**). This is especially relevant in areas with a wide variety of trace orientations, which are usually highlighted with orthogonal "back" azimuths producing enhanced shadows along the scarps. For instance, scarps #1 and #2 are more evident with an azimuth of 135º, whereas this azimuth does hardly show the presence of scarp #5.

We visited zone A1 (**Fig. 9**), and the heights of the scarps measured in the field were consistent with those obtained from the 1 m DEM, calculated by extracting topographic sections across the scarps (similar to the sections presented in **Fig. 11**). A maximum scarp height of about 4 m was measured for scarp #3 in the field, whilst most of the scarps have average heights between 1 and 2 m (**Fig. 9**). The height of about 4 m, however, only corresponds to the fresher trace of the scarp, and not to the ~15 m maximum accumulated offset affecting the planar areas north and south of the scarp. This much larger displacement is indicative of the previous stages of movement, obliterated at other parts of the mountain slope undergoing enhanced erosion. That is, the erosion is expected to be minor at this gentler part of the slope, allowing the preservation of the offset planar landforms. Zone A2 was not visited in the field. Even though the scarps in this area are not visible through aerial photo-interpretation, they are clear in the shaded relief map from the 1 m DEM (**Fig. 7**) and its 3D view (**Fig. 8**).The assemblage of scarps is interpreted as the head scarps (A1) and the middle antislope scarps (A2) of a minor slope deformation (part of a RSF). Hutchinson (1988) proposed to distinguish superficial and slow failures, such as topples, which do not propagate more than 100-150 m deep, from failures affecting deeper zones. Hutchinson (1988) differentiated rotational basal failure surfaces (or zones) from deeper ones showing basal envelopes of deformation with two main surfaces (or zones): a subvertical and dipping downslope one and a subhorizontal one, located near

the base of the slope. We have used this idea to reconstruct the approximate geometry and depth of the basal zone of deformation. This basal surface would be only partly developed. It is plausible that the subhorizontal basal zone is taking advantage of the bedrock foliation planes (features mapped by Poblet, 1991; **Fig. 1**). A synthetic cross section of this slope failure, including these zones, is shown in **Fig. 11** (transect Y–Y' in **Fig. 3**).

The 3D analysis of the scarps in terms of their geometry and position within the slope and that of the slope morphology led us to infer three hypothetical zones of maximum reach of deformation in depth. These three surfaces could be part of the failure; the in-depth continuation of the southernmost head scarp, inferred from the interpolation of the trace of the scarp, is interpreted as a suitable basal deformation-zone controlling the failure (dashed line). We suspect that this surface is not completely developed, since otherwise the slope failure would be in a more advanced stage. However, the geometry of the slope at its lower-middle part and the antislope scarps developed there suggests that there has been some mobilization of the rock mass, at least sufficient to produce the observed bulging (**Fig. 11**).

4.2.2. Zone A3

This landform seems to be the result of an arrested RSF affecting the lower parts of two converging spurs separated by a fluvial incision. The resulting composite head scarp (~600 m-long) has two sub-segments showing a maximum cumulated offset of 25 m at the center of their traces, and offsets smaller than 10 m along most of the scarp. This slope failure cannot be properly detected in the 5 m DEM, or by the analysis of aerial stereo-pairs or orthophotos. Contrary, in the 1 m DEM, this head scarp is clearly observed, allowing the identification of several sub-segments (**Fig. 4**). Only the 3D visualization of this area revealed the mapped extension of the failure (**Fig. 8**). Prior to the 3D visualization, only the westernmost part of the head scarp had been interpreted as a failure landform. Only when observed from distant points, such as the eastern slope of zone A4, it

was possible to identify this RSF in the field. The total mobilized area in this RSF, based on the 1 m DEM, is 0.11 km^2 (**Table 2**).

A topographic profile across this feature (transect X–X' in **Figs. 11** and **3**) shows the apparent dip of the head scarp. In the proposed interpretation of the in-depth continuation of the scarp, the basal deformation zone is subhorizontal under the lower part of the slope, and merges to a step in the slope. Such a change in the slope is most likely indicative of the former base of the local slope, now disturbed by the mobilized mass. This geometry is possibly the result of an arrested RSF, where the displaced mass can be clearly distinguished from the unaffected slope and is capped by a planar area (platform) slightly tilted against the slope.

4.1.3. Zone A4

This area is located between the Portainé valley and the Ramiosa catchment (**Figs. 3** and **4**). In the upper part of this zone, an assemblage of four antislope scarps has been mapped. The uppermost scarp is the largest one (223 m long and 1–2 m high), whilst the other scarps are smaller (60–75 m long and 0.5–2 m high). In the lower part, a single head scarp affects the ridge. This head scarp is 300 m long and shows a maximum height of 3.5 m. All these features are only evident on the bare-earth DEM (**Fig. 4D**). Both the upper and lower parts of this ridge seem to be affected by incipient slope deformation developed perpendicular to the maximum dip of the slope. The slope deformation would be controlled by the extension of the slope towards the north (lower part) and northwest (upper part). This sector was not visited in the field.

4.3. Zone B

This zone corresponds to the Portainé upper valley. Two sets of scarps are differentiated within this zone (**Figs. 3** and **5**). In the field, we inspected zones B2 and B3.

4.3.1. Zones B1 and B2

These zones correspond to the head (B2) and eastern side (B1) of the Portainé upper valley, where part of the ski resort is located. The most prominent feature consists of an arrested RSF involving 0.32 km^2 of mountain ridge, bounded by a well-defined head scarp (B2). This failure had been already identified and mapped by Hartevelt (1969, 1970). The continuation of the head scarp and the failed mass towards the eastern side of the valley (B1) implies an extra area of 0.18 km^2. The top of the RSF is located close to Torreta de l'Orri, affecting part of the Portainé cirque sidewalls and reaching the cirque floor. Scarps within zones B1 and B2 reshape the glacial ridges of the Portainé cirque, whose former location at the S and SE areas can be inferred from the curved shape of the undisturbed ridge to the west (**Figs. 3, 5A** and **5D**). The slipped area is characterized by a bumpy irregular surface (scarps #1, 2 and 4 in **Figs. 5** and **10**). The head scarp of this slipped area (#2 at B2) is 900 m long and 15 m high, and the minor scarps #1 and #2 have maximum heights of 1 and 2 m, respectively, measured both in the field and on the 1 m DEM. All of them are features sharper than the glacial ridges, suggesting that they are younger, i.e. post Last Glacial Maximum. Other scarps in the area are 86–280 m long with maximum heights of 6 m (western rear scarp) and 5–6 m (eastern scarps).

The topographic cross section perpendicular to this slope failure (transect Z-Z' in **Fig. 3**) is shown in **Fig. 11**. The consecutive steps (or breaks in the slope) observable along the mobilized mass are interpreted as the top of sliding blocks. This failure has been interpreted as an arrested RSF that occurred after the Upper Pleistocene Portainé glacier retreated. The prolongation of the main scarp towards the north produced multiple smaller RSFs (arrested type), characterized by the multiple horseshoe shaped scarps, and the associated breaks in the slope observed in zone B1. Active failure of the glacial ridge is evidenced by the presence of two fresh fractures affecting the ridge between the western and central glacial cirques (#3 in **Fig. 10**). These scarps are visible but

not evident in the shaded relief maps from the 1 m DEM, probably because they are short features (18–20 m long), but they are visible in the aerial orthophotos because of the snow infill. They appear as opened fractures ~1 m wide and are oriented N070E to N078E, perpendicular to the main foliation planes but sharing their strike. The mechanism producing these fractures is not straightforward; since they are not parallel to the slope they cannot be interpreted as extensional fractures or topples. We could speculate that they are related to the failure of the entire ridge (glacial cirque) towards the south. A more precise diagnosis of the slope failures in this area requires a further analysis of the geological structure and landforms within these south-facing southern glacial cirques.

4.3.2. Zone B3

Three scarps were identified in this area along the ridge that constitutes the western boundary of the Portainé cirque. The two northern ones are antislope scarps, but their location also indicates that they are ridge top scarps. Their lengths range between 60 and 223 m, showing maximum heights around 1.5 m. Their location and orientation with respect to the Portainé cirque suggest that they are bounding slices of a failing cirque flank. The northern scarps have been interpreted as an open fracture generating a small "double ridge". These scarps were visited in the field. The northernmost scarp (antislope scarp #5 in **Fig. 10**) has an approximate maximum height of 1 m**.**

Scarps in the B1 zone and some of the scarps in the B2 and B3 zones are only detected in the 1 m DEM. In the 5 m DEM and in the aerial orthophotos, only the main head scarp of B2 and the double ridge of B3 are suspected, but they cannot be mapped owing to their small size and the vegetation that covers part of the landforms (**Fig. 5A**).

4. 4. Zone C

The westernmost zone corresponds to the uppermost part of the La Masia catchment (**Figs. 2** and **3**). The area shows a relatively large density of scarps that have been grouped into two subzones

according to their typology and the general sense of the slope movement (**Fig. 6**). The observed deformation does not fit to the single type of mass movement proposed by Hungr et al. (2014), due to their complexity, so we described it as a complex type. The geometric characteristics of the slope failures identified in the Portainé zone and their perceptibility within the aerial photos, the orthophotos and in the 5 m DEM are listed in **Table 2**.

4.4.1. Zone C1

This zone is on a cranked ridge between the Ramiosa and the La Masia streams (**Figs. 2, 3** and **6**). It occupies an area around 1.43 km^2 and is made of two sub-sectors showing different types of scarps: 1) a narrow southern zone (the upper part of the ridge, oriented SSW–NNE), which is affected by a sequence of slope failures, characterized by horseshoe shaped head scarps, and by shorter and smaller scarps developed within the affected slope, and 2) the area below (to the north), which represents a lower part of the slope and the continuation of the ridge towards the NW. This area shows several ridge top scarps that extend up to the Roques d'Auló peak (1742 m a.s.l.) and are developed on both sides of the watershed. At Roques d'Auló, a double ridge has been developed defining a closed depression of 37 m width. Only some segments of these scarps can be inferred if the 5 m DEM is used, whereas their traces can be clearly mapped using the 1 m DEM. The area is mostly covered by forest with the exception of its southwestern tip, where the larger head scarps are distinguished in the orthophotos (**Fig. 6A**). The maximum heights of the scarps do not exceed 5 m (commonly between 2.5 and 3 m; some of the scarp heights are detailed in caption of **Fig. 6**). In the field, a selection of these scarps was visited (photographs are included in Supplementary Material 7). Their small heights and the high roughness of the terrain make their identification difficult. The surface is generally very bumpy and irregular, and has been partially modified by forestry works. Only the scarps showing more rectilinear traces can be distinguished from other surface irregularities. At the boundary between the zones C1 and C2, a downthrown planar area, aligned

with the ridge and bounded to the west by scarp #4, stands out as the most evident feature (Supplementary Material 7). This scarp has a maximum height of ~0.5 m and shows a very sinuous winding trace.

The bedrock weathering in this area seems to be greater than for the other zones studied here (more than 10 m thick as seen at some outcrops), and hinders the detection of failures. A topographic cross section along the slope of C1 zone (section WW' in **Figs. 3** and **11**) shows the location of the main scarps with respect to the slope profile. In the uppermost part, the type of movement seems strongly controlled by the presence of the thick colluvium and by the dip and orientation of the tectonic foliation (**Fig. 1**), which could define the location of superficial and deeper basal sliding planes. According to the observed morphologies, the most likely failure mechanism is a complex movement to the NE, probably as a result of the large increase in slope towards the Ramiosa valley (**Figs. 3** and **6**). This complex failure is a combination of 1) a deformation of colluvium dominated by a slow flow along low dipping (< 12º) basal surfaces in the SW-NE ridge; the shallow nature of this movement is inferred from the close shape of the arcuate head scarps, and 2) scarps produced by RSFs, perhaps superficial features such as rock flexural topples or extensional fractures. The NE slope in this sector is larger (~28°).

The fact that the scarps are traceable within the colluvium suggests that the failure is relatively young (after the Last Glacial Maximum) and even active. Otherwise, the re-distribution of the soil cover would have obliterated the presence of the scarps. Our interpretations, however, are preliminary, since they are based only on the observation of very subdued landforms in a very irregular terrain. No clear crosscutting relationships are detected between the different head scarps, and their simultaneous activity cannot be ruled out.

4.4.2. Zone C2

This area corresponds to a bumpy hillslope with a general slope of ~22º towards the NW. The scarps are mainly parallel to the slope direction, are very discontinuous and have a sinuous form. Most of them are lineaments defined by small ridges, so it is not straightforward to correlate the areas located at both sides of the scarps. In other words, these areas have a different appearance across the scarp perhaps as a consequence of a loss of structure in the downslope slid zone. The length of the scarps ranges between a few meters and a maximum of 273 m and their height ranges between <1 to 5 m. Most of the scarps are only detected in the 1 m DEM, and none of them is visible in the aerial orthophotos. Only a few scarps were visited in the field (#5 and 6 in **Fig. 6**). As in zone C1, they are hard to distinguish due to the roughness of the terrain.

This zone is also characterized by a thick colluvium and is especially affected by ongoing superficial creep leading to distortion of trunks. The sinuosity of the scarp traces leads us to interpret the assemblage as a result of slope creep towards the NW. The material involved in the flow is a weathered regolith, but this does not fit with the idea of "clayey soil" considered in the classification of mass movements proposed by Hungr et al. (2014). The observed small displacements suggest it is a slow movement (<1 cm $year^{-1}$) at its initial stage. Some of the straighter scarps could also be related to extensional failures and/or toppling.

Although zones C1 and C2 have been interpreted independently according to the general sense of the slope movement, the entire ridge seems to be collapsing in some kind of radial extension, with the Raimosa valley side spreading to the NE and the La Masia valley to the NW.

To the NW, several RSFs can be inferred at the left margin of the Noguera Pallaresa valley. They have not been studied in this work, but their preliminary mapping has been included in Supplementary Material 7. Since they are located in a different part of the ridge and ~1.5 km away from zone C2, we have not considered these landforms as part of the same slope failure.

5. Discussion

5.1. LiDAR mapping of subdued landforms of slope failure within forested areas

Most publications on landslide detection using LiDAR derived DEMs dealt with areas where several landslides had been detected (Haugerud et al., 2003; Schulz, 2004; Ardizzone et al., 2007; Van Den Eeckhaut et al., 2007 and 2011; Lin et al., 2013; Razak, 2014). In this paper, the LiDAR data analysis is implemented for the first time in an area where only one large landslide had been reported by Hartevelt (1969, 1970). None of the other slope failures (RSFs and colluvium deformations) existing in this area, had been detected due to the weak topographical and morphological expression of the associated features and to their location under the forest canopy. The results show that high-resolution LiDAR-derived topographic images are a powerful tool, allowing the detection and characterization of subdued large-scale slope failures even in forested areas.

To deal with subdued failures with limited visible expression, the use of high-resolution (sub 5 m) topography might be the only tool to detect and map the associated landforms, because subdued landslide features might not be visible in aerial photographs including orthophotos, unless the scarps are distinct, for instance, by lineations of contrasting vegetation. Moreover, their continuity is hard to be detected in field surveys especially inside the forest, and they can be misunderstood by lack of contextualization. These subdued landforms could be associated with old eroded slope failures, but also with slope deformations at an early stage. The early detection of slope failures is particularly relevant to hazard prevention, e.g. they could rapidly evolve into catastrophic landslides (Brückle and Parotidis, 2005). Moreover, they can also be critical, even if moving slowly, when planning infrastructures like tunnels, dams or roads.

In this paper, we have shown that most of the scarps with heights of 0.4 to 1 m are identifiable using images from the 1 m DEM. Moreover, many other scarps, with larger heights, are only detectable in the 1 m images due to their location under the forest canopy. Table 2 summarizes the geometrical characteristics of the scarps within the different studied zones, including the interpreted

failure mechanism, and if they are detectable or not using the DEMs with different resolutions and the aerial photographs. The table indicates that LiDAR data emerge as a key tool for completing the inventories of mass movements within the Pyrenees and other mountainous regions.

5.2 Incompleteness of geomorphological inventories

The main problems associated with the generation of high quality landslide inventories are: 1) difficulties in achieving completeness because of the lack of particular data sets, such as LiDAR DEMs and geological maps; 2) lack of adequate training of technicians and scientists devoted to landslide detection and interpretation, and 3) concentration of studies in specific areas, such as those where previous catastrophic slope failures have occurred. For example, in the Pyrenees, Corominas and Baeza (1992) studied the Pont de Bar landslide, which has been moving an entire village, and Gutiérrez et al. (2008) and Zarroca et al. (2014) focused on slope failures in the epicentral areas of the 1373 Ribagorça earthquake (estimated in M_w = 6.2 + 0.5 by Olivera et al., 2006).

The completeness of a landslide inventory will determine its potential to: 1) generate landslide susceptibility, hazard and risk maps (Van Den Eeckhaut and Hervás, 2012), and 2) infer the role of the main controlling and triggering factors of mass movements to properly understand slope failures. As noted by Malamud et al. (2004), a functional complete catalogue must reflect the natural dominance of smaller slope failures over the larger ones. This dominance is not reflected in historical inventories, since the smallest landforms tend to be rapidly obliterated by erosion, covered by sediments or hidden under the vegetation. With the implementation of modern techniques, the incorporation of subtle landslides into geomorphological inventories may be improved. In this sense, the use of LiDAR mapping is crucial because it enables the detection of small and subdued failures.

The lack of a specific background in the study of some RSF types is likely to be a key issue in the hypothetical underrepresentation of slope deformations within the maps and reports of slope

failures for the Pyrenees. For instance, the Slope Deformation type (which includes the DGSD type) is not incorporated in the official geomorphological maps of Spain at any scale (Martín-Serrano et al., 2004), and its research in the Pyrenees only date back to the 1980s (see Section 1.3). This situation is very different from other countries with alpine relief such as Switzerland or Italy, where they count with more than 40 years of background in the mapping of phenomena like DGSDs. These have been extensively mapped, and tenths of publications have reported a large number of deep-seated slope failures (e.g., Zischinsky, 1966; Nemčok, 1972; Forcella, 1984; Ambrosi and Crosta, 2006; APAT, 2007; Aringoli et al., 2013). We infer that the noticeable lower presence of DGSDs in the Pyrenean inventories is more likely due to the lack of geomorphological background of the compilers than to a real absence in the terrain.

In the present work, we deal with large-scale slope failures not documented in previous works in spite of the existing regional maps of the area (Hartevelt, 1969, 1970) and previous technical reports (ICGC, 2012, 2013). This situation is likely to be frequent in many other areas of the Pyrenean range. We are convinced that the systematic survey of wide areas by the analysis of LiDAR derived maps would show a much larger number of large-scale slope failures by adding the incipient landforms to the ones already detected. Only by achieving this completeness, a proper evaluation of the spatial controlling factors of these slope failures can be performed.

5.3. Controlling and triggering factors of large-scale slope failures

The slopes in Portainé are characterized by weakened rocks, which result from intense tectonic deformation and enhanced weathering. The landscape here is mainly the consequence of fluvial and slope processes that entrench the smooth Late Miocene landscape. According to the terminology proposed by Jarman et al. (2014), zones A and C correspond to the parafluvial domain, referring to the areas belonging wholly or partially to fluvial valleys where slope failures are not directly provoked by, or linked to, river erosion. Slope failures in zones A and C were not caused by direct

active river erosion at their toes, but were rather affected by the slope change related to fluvial entrenching. This could be an indicator of a localized disturbance to steady-state conditions of the slopes.

Three different slope angles are present: an upper zone with gentle slopes (<10°) corresponding to the preserved patches of preglacial summit surface remnants; a middle zone with medium slope values (10–20°) controlled by local slope processes such as superficial runoff and slope failures, (with the exception of glacial cirques with more pronounced relief); and a lower zone with greater slope angles (20–35°) due to Plio-Quaternary fluvial incision. This downward increase in the slope angle and the terrain convexity in the transition zones produce a lack of lateral and basal support to the upper slope, enhancing the gravitational stress through the mountain ridge, leading to the instability of the uppermost parts. The areas affected by slope failures are the upper and middle ones, and most of them are related to terrain convexities and even affect some preglacial summit surfaces.

The summit surfaces are more prone to RSFs and other slope failures than sharper crests and horns. This is well known from both theoretical work (Gerber and Scheidegger, 1969) and field observations (Beck, 1968). Jarman et al. (2014) also found a significant association between RSFs and such surfaces in the Eastern Pyrenees. We did not detect many RSFs in the lowermost areas, which might be the result of fluvial incision, obliterating them, or because they are hidden under the thick colluvium.

For the larger RSF located within the Portainé cirque (zone B, #1–3), the steepening of the headwall by glacier erosion sculpturing the glacier cirque seems to be the major cause of slope instability, since the failure is limited to the area occupied by the cirque glacier and affects glacial landforms. This RSF is thus located in the paraglacial domain, following the ideas of Ballantyne (2002). For the subdued slow flow of colluvium (zone C1) and for the creep (zone C2), the presence of thick colluvium, resulting mainly from periglacial action, is considered as a relevant controlling

factor. The slow flow of colluvium, in particular, seems to be occurring along foliation surfaces sub-parallel to the slope and dipping towards the north, in agreement with the elongation of the affected mass and the geometry of the sliding surface inferred from the trace of the head scarps (**Figs. 1** and **6**).

The variable roughness of the slope failure landforms in Portainé suggests that they generated asynchronously. Some of the landforms, such as those in zone A3, are subdued and could have been generated even before the Last Glacial Maximum. Contrarily, the sharpness of landforms such as the scarps in zone A1, as inferred from the LiDAR analysis and observation in the field, suggests recent activity of the failures. Although we cannot directly obtain the age of the scarps, we suppose that they are younger than those studied by Gutiérrez et al. (2008) in the Central Pyrenees (Ubago site at Sierra Negra), which are significantly smoother and moved since 8.3–5.3 ka and affected similar lithologies and slope angles.

In the area around the Noguera Pallaresa River close to Portainé, within 10 km from Rialp village along the Àssua and the Noguera Pallaresa valleys, a cluster of slope failures is noticed. In contrast to Portainé, most slope failures are located in non-forested areas or they present large and evident morphologic expression. All of them are located in the parafluvial domain and most of them affected summit surface remnants. A summary is shown in Table 3 and their approximate location is shown in **Fig. 1**. Not all these slope failures are synchronous and many of them suffered reactivations, some even in present times (Furdada, 1988; Furdada and Vilaplana, 1988). Regarding their age, two significant RSFs cut and overlap fluvioglacial terraces: the La Bastida (~20 m above the valley floor; 2 km south of Rialp) and the La Gessera, south of Sort (~35 m above the valley floor; 5.5 km south of Rialp) (**Fig. 1** and Supplementary Material 6). Although these fluvioglacial terraces are undated, Furdada (1988) compared the La Bastida RSF with the terraces described by Vilaplana (1983) in the adjacent Noguera Ribagorçana basin, and correlate it to the beginning of the deglaciation phase. Turu et al. (2011) state that the Noguera Pallaresa glacier was the most

extensive one in the Southern Pyrenees during the Last Glacial Maximum, with its front located between Sort and Llavorsí. Among other deposits, they describe fluvial terraces downstream from Sort at 20 m and 30–40 m above the valley floor as corresponding to their T7 and T6 levels, respectively, and indicate their probable relation to the last maximum ice extent. This would imply an entrenchment of the Noguera Pallaresa River of 20 to 40 m since the last deglaciation. The heights of these terraces and their age interpretations are quite consistent, even though more precise dating is needed. The two large RSFs that cut and overlap the La Bastida and La Gessera fluvioglacial terraces might have formed during a disequilibrium phase around the last deglaciation related to the subsequent river incision because they cut these terraces and the sliding planes are located at 20 to 35 m above the present valley floor (Supplementary Material 6). This is coherent with the interpretations of Jarman et al. (2014), who indicate that the montane RSFs in the Eastern Pyrenees could reflect a phase of disequilibrium around the last deglaciation.

However, RSFs in the Eastern Pyrenees seem to be sparse compared to the area we studied here in the Central Pyrenees. Jarman et al. (2014) interpret that the sparse, subdued RSFs they describe in the Eastern Pyrenees are evidence of relative tectonic stability and low intensity glaciation. Moderate values of uplift rates experienced in the Eastern and Central Pyrenees since the Upper Miocene (around 0.2 mm yr^{-1} for the Eastern part, Calvet and Gunnell, 2008; between 0.08 and 0.19 mm yr^{-1} for the central part, Ortuño et al., 2013) suggest that the differences in RSFs distribution between these regions must be a response to additional factors rather than just differential uplift.

Another issue to consider is the effective base level controlling incision. Gunnell et al. (2009) affirm that the primary driving force behind fluvial incision in the Eastern Pyrenees is Neogene tectonic uplift. However, its effectiveness is dependent on the connectivity of the drainage systems to drops in regional and local base levels (Jarman et al., 2014). In the Eastern Pyrenees, the elevated semi-internal basins of Cerdagne and Capcir set local base levels to surrounding massifs at ~1200–1600 m a.s.l. (Jarman et al., 2014). In the Noguera Pallaresa basin, these local base levels do not

exist, thus fluvial incision could be more effective and also the related slope disequilibrium and consequent RSF.

Another RSF controlling factor can be attributed to geology. The RSFs cluster around the study area is located along the several regional thrusts bounding the Orri thrust-sheet (**Fig. 1**). Such cases might have a clear geological control, since the outcropping rocks are commonly associated to weaker mechanical properties. For instance, RSFs in the Àssua valley occurred in Silurian black slates, rich in graphite, and the La Bastida and La Gessera RSFs occur along a major alpine thrust involving Permo-Triassic rocks with Buntsandstein facies (including clays and gypsum, supplementary material 6). These lithologies are known to facilitate the failure of the slopes and have been associated to slope failures in other sectors of the Pyrenees (e.g., Furdada and Vilaplana, 1988, Hürliman et al., 2006).

All these controlling factors, i.e. moderate tectonic uplift, the disequilibrium phase around the last deglaciation, subsequent enhanced fluvial incision due to lowering of local base levels, and the particular geological context can explain the slope failure cluster in the parafluvial domain related to the Portainé area slope failures. Slope failures could have started before the last glacial cycle; while during the deglaciation disequilibrium phase they could have been reactivated or new ones could have been generated.

Additionally, the role of the regional seismicity and climate during the Plio-Quaternary might have contributed to the slope instability. With respect to the seismic trigger, it is worth to highlight that the Portainé area is located 40 km east from the epicenter of the largest historical earthquake recorded in the Central Pyrenees, the 1373 Ribagorça earthquake (Mw 6.2 ±0.5; Olivera et al., 2006), with related landslide activity (Gutiérrez et al., 2015; Olivera et al., 2006; Zarroca et al., 2014). Given the 25 km uncertainty of the epicenter location reported by Olivera et al. (2006), the studied area could be situated even closer to it. Moreover, the Portainé area is less than 50 km apart from the known neotectonic faults in the Pyrenees summarized by Lacan and Ortuño (2012): the

Urgellet fault, 14.5 km to the SE; the Cerdanya fault, 42 km to the SE; the Merens fault, 37 km to the NE; and the Rius-Cabanes and North Maladeta fault, 25-30 km to the NW (**Fig. 1B**).

Although there are no specific glacial studies for the Portainé area, the early works by Hartevelt (1969, 1970) and the general morphology lead us to consider that, besides the Portainé cirque, the studied ridges were not covered or adjacent to any glacier during the Last Glacial Maximum. Holocene climatic phases with enhanced precipitation however, are likely to have led to slope instability, as inferred by Lebourg et al. (2014) for a sector of the Western Pyrenees.

6. Conclusions

This work provides the results of a pilot study performed in the upper slopes of a restricted mountain area (60 km^2), in which the interpretation of LiDAR derived maps has been shown to be crucial to identify landforms associated with subdued slope failures, such as scarps less than1 m high, with limited visible expression. This has been especially relevant to landforms located under the forest, and thus, hard to detect by conventional mapping methods. It is noteworthy that some of the scarps detected in this work are associated with superficial slope failures affecting the colluvium, which are more difficult to observe due to their smoother shapes in comparison with the landforms associated with RSFs. Therefore, LiDAR data provide key information, contributing to improve the completeness of slope failure inventories.

The presence of vegetation and the steep terrain are limiting factors reducing the precision of LiDAR derived datasets in mountain areas that can be overcome by specific data collection flights and by trained operators' data processing. The inspection of differently illuminated shaded-relief and contour maps in 2D and 3D visualizations allows us to detect landforms associated with subtle slope failures and to observe assemblages of a large number of features along extensive areas. Expert-based analysis, even though introducing subjectivity, is shown to be indispensable for

the identification of subtle landforms associated with subdued or small-scale slope failures in this pilot study.

In the Portainé study area, a high density of scarps related to slope failures was identified on the remnants of a Neogene summit surface and its surroundings. These were identified for the first time by analyzing 1 m resolution LiDAR derived images. The main reason why the scarps are detectable in the bare-earth DEMs is their spatial continuity, since their vertical displacements are often undetectable on a set of topographic profiles.

The analysis of the scarp assemblage led us to classify the slope failures as large-scale failures, i.e. larger than 0.25 km^2, and belonging to a variety of types: four cases of RSF (two arrested RSF and two slope deformations), and a complex slide combining slow flow (affecting colluvium) and slope deformation. Several isolated scarps could be produced by toppling or lateral extension. The freshness of the landforms and the fact that they are locally displacing features of the Last Glacial Maximum (LGM) suggest that the last phase of activity is post-LGM and probably the late Holocene, with enhanced incision of the fluvial drainage being the main controlling factor. We observed that: 1) most slope failures are in the parafluvial domain, i.e., they occurred in relation with the over-steepening of the slopes related with fluvial processes, and 2) slope failure is concentrated along the paleic summit surface rims, which appear particularly susceptible (zones A1, B1, 2, 3 and C1).

The case study presented here might serve as a reference work when deciding if the use of LiDAR high-resolution data might help to detect small size scarps within a similar mountainous area. The implementation of LiDAR data analysis should reveal the existence of many more areas affected by subdued large-scale slope failures, especially in mountainous regions, improving the quality of slope failure inventories and the understanding of slope failures. This could be achieved by a systematic survey of a large region performed by trained geomorphologists, allowing more

accurate discussion on the controlling factors of slope failures, such as slope morphology, climate, seismicity, tectonics and hydrology.

Acknowledgments

This work was supported by the AGAUR 2009-SGR-520 funding of the RISKNAT group, the CHARMA Spanish Project (MINECO, Ref.: CGL2013-40828-R) and the funds of the Institut Cartogràfic i Geològic de Catalunya (ICGC) for the acquisition and processing of LiDAR data. We are indebted with David Jarman for his careful and thorough revision, which has led to a substantial improvement of the work presented. We also thank Veronica Náquira for helping with the photo-interpretation blind test and field assistance.

References

Agliardi, F., Crosta, G., Zanchi, A., 2001. Structural constraints on deep-seated slope deformation kinematics. Eng. Geol. 59, 83–102. doi:10.1016/S0013-7952(00)00066-1

Ambrosi, C., Crosta, G.B., 2006. Large sackung along major tectonic features in the Central Italian Alps. Eng. Geol. 83, 183 – 200. doi:10.1016/j.enggeo.2005.06.031

APAT, 2007. Rapporto sulle frane in Italia. Il Progetto IFFI – Metodologia, risultati e rapporti regionali. Rapporti n. 78/2007. Dipartamento difesa del suolo.

Ardizzone, F., Cardinali, M., Galli, M., Guzzetti, F., Reichenbach, P., Irpi, C.N.R., Alta, M., 2007. Identification and mapping of recent rainfall-induced landslides using elevation data collected by airborne Lidar. Nat. Hazards Earth Syst. Sci. 7, 637–650. doi:10.5194/nhess-7-637-2007

Aringoli, D., Gentili, B., Materazzi, M., Pambianchi, G., Sciarra, N., 2013. DSGSDs induced by post-glacial decompression in Central Apennine (Italy). Landslide Sci. Pract. Glob. Environ. Chang. 4, 417–423. doi:10.1007/978-3-642-31337-0_54

Axelsson, P., 2000. DEM generation from laser scanner data using adaptive TIN models. Int. Arch. Photogramm. Remote Sens. 35, 236–241.

Babault, J., Van Den Driessche, J., Bonnet, S., Castelltort, S., Crave, A., 2005. Origin of the highly-elevated Pyrenean peneplain. Tectonics 24, 1–19. doi:10.1029/2004TC001697

Bachmann, D., Bouissou, S., Chemenda, A., 2009. Analysis of massif fracturing during Deep-Seated Gravitational Slope Deformation by physical and numerical modeling. Geomorphology 103, 130–135. doi:10.1016/j.geomorph.2007.09.018

Ballantyne, C.K., 2002. Paraglacial geomorphology. Quaternary Science Reviews, 21, 1935–2017.

Beaumont, C., Muñoz, J.A., Hamilton, J., Philippe, F., 2000. Factors controlling the Alpine evolution of the central Pyrenees inferred from a comparison of observations and geodynamical models. J. Geophys. Res. B Solid Earth Planets 105, 8121–8141.

Beck, A.C., 1968. Gravity faulting as a mechanism of topographic adjustment. New Zealand Journal of Geology and Geophysics, 11 (1), 191-199.

Bennett, R., Welham, K., Hill, R.A., Ford, A., 2012. A Comparison of Visualization Techniques for Models Created from Airborne Laser Scanned Data. Archaeol. Prospect. 19, 41–48. doi:10.1002/arp

Boissevain, H., 1934. Étude géologique et géomorphologique d'une partie de la haute vellée du Segre (Pyrénées Catalanes). Bull. Soc. Hist. Nat. Toulouse LXVI, 32–170.

Booth, A.M., Roering, J.J., Perron, J.T., 2009. Automated landslide mapping using spectral analysis and high-resolution topographic data: Puget Sound lowlands, Washington, and Portland Hills, Oregon. Geomorphology 109, 132–147. doi:10.1016/j.geomorph.2009.02.027

Bordonau, J., Vilaplana, J.M., 1986. Géomorphologie et tectonique récente dans le Val d'Aran (zone axiale des Pyrénées Centrales, Espagne). Rev. Géologie Dyn. Géog. Phys. 27, 303–310.

Briais, A., Armijo, R., Winter, T., Tapponnier, P., Herbecq, A., 1990. Morphological evidence for Quaternary normal faulting and seismichazard in the Eastern Pyrenees. AnnalesTectonicae 4, 19–42.

Brückle, E., Parotidis, M., 2005. Prediction of slope instabilities due to deep-seated gravitational creep. Nat. Hazards Earth Syst. Sci. 5, 155–172. doi:10.5194/nhess-5-155-2005

Burman, H., 2000. Calibration and orientation of airbone image and laser scanner data using GPS and INS. Royal Institute of Technology.

Calvet, M., 1999. Régimes des contrainteset volumes de relief dans l'est des Pyrénées. Géomorphologie Reli. Process. Environ. 5, 253–278.

Calvet, M., Gunnell, Y., 2008. Planar landforms as markers of denudation chronology: an inversion of East Pyrenean tectonics based on landscape and sedimentary basin analysis. In: Gallagher, K., Jones, S.J. and Wainwright, J. (eds), Landscape Evolution: Denudation, Climate and Tectonics Over Different Time and Space Scales. Geological Society, London, Special Publication, 296, 147–166.

Calvet, M., Delmas, M., Gunnell, Y., Braucher, R., Bourlès, D., 2011. Recent advances in research on Quaternary glaciations in the Pyrenees. In: Ehlers, J. and Gibbard, P.L. (eds), Quaternary Glaciations, Extent and Chronology, A Closer Look. Part IV. Elsevier, Amsterdam. 127–139.

Carozza, J.M., Baize, S.M., 2004. L'escarpement de faille de la Têt est-il le résultat de la tectonique active Plio-Pléistocène ou d'une exhumation Pléistocène ComptesRendus. Geosciences 336, 217–226. doi:10.1016/j.crte.2003.10.026

Corominas, J., Baeza, C., 1992. Landslide occurrence in Eastern Pyrenees. In: Del Prete, M. (ed.), Movimenti franosi e metodi di stabilizzazione. Consiglio Nazionalle delle Ricerche, Publicazione 481, 25–42.

CREAF, 2009. Mapa de cobertes de sòls de Catalunya. Centre de Recerca Ecològica i Aplicacions Forestals. Universitat Autònoma de Barcelona.

Crosta, G.B., 1996. Landslide, spreading, deep seated gravitational deformation: analysis, examples, problems and proposals. Geogr. Fis. e Din. Quat. 19, 297–313.

Crosta, G.B., Clague, J.J., 2006. Large landslides: Dating, triggering, modelling, and hazard assessment. Eng. Geol. 83, 1–3. doi:10.1016/j.enggeo.2005.06.023

Derron, M.-H., Jaboyedoff, M., 2010. Preface "LIDAR and DEM techniques for landslides monitoring and characterization." Nat. Hazards Earth Syst. Sci. 10, 1877–1879. doi:10.5194/nhess-10-1877-2010

Devereux, B.J., Amable, G.S., Crow, P., 2008. Visualisation of LiDAR terrain models for archaeological feature detection. Antiquity 82, 470–479. doi:http://dx.doi.org/10.1017/S0003598X00096952

Dramis, F., Sorriso-Valvo, M., 1994. Deep-seated gravitational slope deformations, related landslides and tectonics. Eng. Geol. 38, 231–243.

ESRI, 2016. ESRI [WWW Document]. URL http://www.esri.com/

Evans, G.E., Clague, J.J. , 1996. Recent Climatic Change and Catastrophic Geomorphic Processes in the Mountain Environments. Geomorphology, 10, 107-128.

Forcella, F., 1984. The sackung between Mount Padrio and Mount Varadega, Central Alps, Italy: a remarkable example of slope gravitational tectonics. Mediterranee 51, 81–92.

Furdada, G., 1988. Estudi Geomorfològic de la Vall d'Àssua i marge dret de la ribera de Sort (Pallars Sobirà). Tesi de Llicenciatura. Dpt. Geologia Dinàmica, Geofísica i Paleontologia; Universitat de Barcelona. Unpublished. 182 pp and 1 map.

Furdada, G., Vilaplana, J.M. 1988. Grandes deslizamientos en las laderas de la Vall d'Àssua y margen derecho de la ribera de Sort (Alta cuenca de la Noguera Pallaresa). In: Alonso and Corominas (eds.) Extended abstract of the I Symposium on Slope Instabilities (I Simposio sobre Taludes y Laderas Inestables). Andorra. 1-12.Gerber, E., Scheidegger, A.E. 1969. Stress-induced weathering of rock masses. Eclogae Geologicae Helvetiae, 62 (2), 401-415.

Glenn, N.F., Streutker, D.R., Chadwick, D.J., Thackray, G.D., Dorsch, S.J., 2006. Analysis of LiDAR-derived topographic information for characterizing and differentiating landslide morphology and activity. Geomorphology 73, 131–148. doi:10.1016/j.geomorph.2005.07.006

Gunnell, Y., Calvet, M., Brichau, S., Carter, A., Aguilar, J.P., Zeyen, H., 2009. Low long-term erosion rates in high-energy mountain belts: Insights from thermo- and biochronology in the Eastern Pyrenees. Earth Planet. Sci. Lett. 278, 208–218. doi:10.1016/j.epsl.2008.12.004

Gutiérrez, F., Ortuño, M., Lucha, P., Guerrero, J., Acosta, E., Coratza, P., Piacentini, D., Soldati, M., 2008. Late Quaternary episodic displacement on a sackung scarp in the central Spanish Pyrenees. Secondary paleoseismic evidence? Geodin. Acta 21, 187–202. doi:10.3166/ga.21.187-202

Gutiérrez, F., Linares, R., Roqué, C., Zarroca, M., Rosell, J., Galve, J.P., Carbonel, D., 2012. Investigating gravitational grabens related to lateral spreading and evaporite dissolution subsidence by means of detailed mapping, trenching, and electrical resistivity tomography (Spanish Pyrenees). Lithosphere 4, 331–353. doi:doi: 10.1130/L202.1

Gutiérrez, F., Linares, R., Roqué, C., Zarroca, M., Carbonel, D., Rosell, J., Gutiérrez, M., 2015. Large landslides associated with a diapiric fold in Canelles Reservoir (Spanish Pyrenees): Detailed geological–geomorphological mapping, trenching and electrical resistivity imaging. Geomorphology 241, 224–242.

Gutiérrez-Santolalla, F., Acosta, E., Rios, S., Guerrero, J., Lucha, P., 2005. Geomorphology and geochronology of sackung features (uphill-facing scarps) in the Central Spanish Pyrenees. Geomorphology 69, 298–314. doi:10.1016/j.geomorph.2005.01.012

Guzzetti, F., Mondini, A.C., Cardinali, M., Fiorucci, F., Santangelo, M., Chang, K.T., 2012. Landslide inventory maps: New tools for an old problem. Earth-Science Rev. 112, 42–66. doi:10.1016/j.earscirev.2012.02.001

Hartevelt, J.J.A., 1969. Geological Map of Central Pyrenees. Sheet 10. Esc. 1:50.000.

Hartevelt, J.J.A., 1970. Geology of the Upper Segre and Valira Valleys, Central Pyrenees, Andorra, Spain. Leidse Geol. Meded. 45, 167–236.

Haugerud, R.A., Harding, D.J., Johnson, S.Y., Harless, J.L., Weaver, C.S., Sherrod, B.L., 2003. High-resolution lidar topography of the Puget Lowland, Washington - A bonanza for earth science. GSA Today 13, 4–10. doi:10.1130/1052-5173(2003)13<0004:HLTOTP>2.0.CO;2

Heritage, G.L., Large, A.R.G., 2009. Laser Scanning for the Environmental Sciences. Wiley-Blackwell.

Hippolyte, J.C., Bourlès, D., Léanni, L., Chauvet, F., Lebatard, A.E., 2012. 10Be ages reveal > 12ka of gravitational movement in a major sackung of the Western Alps (France). Geomorphology 171-172, 139–153. doi:10.1016/j.geomorph.2012.05.013

Hungr, O., Leroueil, S., Picarelli, L., 2014. The Varnes classification of landslide types, an update. Landslides 11, 167–194. doi:10.1007/s10346-013-0436-y

Hürlimann, M., Ledesma, A., Corominas, J., Prat, P.C., 2006. The deep-seated slope deformation at Encampadana, Andorra: Representation of morphologic features by numerical modelling. Eng. Geol. 83, 343–357.

Hutchinson, J.N., 1988. General Report: Morphological and Geotechnical Parameters of Landslides in Relation to Geology and Hydrogeology. En: C. Bonnard (Editor), International Symposium on Landslide, Lausanne, Switzerland, 3-35.

Hutchinson, J.N., 1995. Deep-seated movements on slopes. Memorie della societa geologica italiana, 50, 149-166.

ICGC, 2012. Avaluació hidrològica i geològica preliminar de l'estat actual dels barrancs del vessant nord del Pic de l'Orri i de la carretera de Roní a Portainé (Rialp) (No. AO-003/12). Barcelona.

ICGC, 2013. Avaluació de la dinàmica torrencial del torrent de Portainé (No. AP-035/13). Barcelona.

Jaboyedoff, M., Oppikofer, T., Abellán, A., Derron, M., Loye, A., Metzger, R., Pedrazzini, A., 2010. Use of LIDAR in landslide investigations: a review. Nat. Hazards 61, 5–28. doi:10.1007/s11069-010-9634-2

Jarman, D. 2006. Large rock slope failures in the Highlands of Scotland: Characterisation, causes and spatial distribution. Engineering Geology, 83, 161- 182.

Jarman, D., Calvet, M., Corominas, J., Delmas, M., Gunnell, Y., 2014. Large-Scale Rock Slope Failures in the Eastern Pyrenees : identifying a sparse but significant population in paraglacial and parafluvial contexts. Geogr. Ann. Ser. A, Phys. Geogr. 96, 357–391. doi:10.1111/geoa.12060

Kasai, M., Ikeda, M., Asahina, T., Fujisawa, K., 2009. LiDAR-derived DEM evaluation of deep-seated landslides in a steep and rocky region of Japan. Geomorphology 113, 57–69. doi:10.1016/j.geomorph.2009.06.004

Konsoer, K.M., Kite, J.S., 2014. Application of LiDAR and discriminant analysis to determine landscape characteristics for different types of slope failures in heavily vegetated, steep terrain: Horseshoe Run watershed, West Virginia. Geomorphology 224, 192–202. doi:10.1016/j.geomorph.2014.06.030

Korup, O., 2006. Effects of large deep-seated landslides on hillslope morphology, western Southern Alps, New Zealand. J. Geophys. Res. 111. doi:10.1029/2004JF000242

Lacan, P., Ortuño, M., 2012. Active Tectonics of the Pyrenees: A review. J. Iber. Geol. 38, 9–30. doi:10.5209/rev_JIGE.2012.v38.n1.39203

Lebourg, T., Zerathe, S., Fabre, R., Giuliano, J., Vidal, M., 2014. A Late Holocene deep-seated landslide in the northern French Pyrenees. Geomorphology 208, 1–10. doi:10.1016/j.geomorph.2013.11.008

Lin, M.-L., Chen, T.-W., Lin, C.-W., Ho, D.-J., Cheng, K.-P., Yin, H.-Y., Chen, M.-C., 2013. Detecting Large-Scale Landslides Using Lidar Data and Aerial Photos in the Namasha-Liuoguey Area, Taiwan. Remote Sens. 6, 42–63. doi:10.3390/rs6010042

LLISCAT [on line] Data base on terrain movements. ICGC-UPC-IEC. [consulted the 1/07/2016]. URL:http://www.icgc.cat/en/Public-Administration-and Enterprises/Tools/Catalogues/Esllavissades-LLISCAT

Malamud, B.D., Turcotte, D.L., Guzzetti, F., Reichenbach, P., 2004. Landslide inventories and their statistical properties. Earth Surf. Process. Landforms 29, 687–711. doi:10.1002/esp.1064

Martín-Serrano, A., Salazar, A., Nozal, F., Suárez, A., 2004. Mapa geomorfológico de España e. 1:50.000. Guía para su elaboración. Instituto Geológico y Minero de España, Madrid.

McKean, J., Roering, J., 2004. Objective landslide detection and surface morphology mapping using high-resolution airborne laser altimetry. Geomorphology 57, 331–351. doi:10.1016/S0169-555X(03)00164-8

Mora, O.E., Liu, J., Lenzano, M.G., Toth, C., Grejner-Brzezinska, D.A., 2015. Small Landslide Susceptibility and Hazard Assessment Based on Airborne Lidar Data. Photogramm. Eng. Remote Sens. 81, 239–247. doi:10.14358/PERS.81.3.239

Muñoz, J.A., 1992. Evolution of a continental collision belt: ECORS-Pyrenees crustal balanced cross-section, in: McClay, K.R. (Ed.), Thrust Tectonics. Chapman and Hall, London, pp. 235–246.

Náquira, M.V., 2016. Comparison between conventional methods and interpretation of LiDAR data for analysis of landslides in the Central Pyrenees. Unpublished Msc thesis. Universitat de Barcelona, 25 pp.

Nemčok, A., 1972. Gravitational slope deformation in high mountains, in: 24th Int. Geol. Cong., Montreal. Montreal, pp. 132–141.

Ojeda, J.C., 2012. Plan Nacional de Ortofotografía Aérea. XV Congreso Nacional de Tecnologías de la Información Geográfica. 19-21 sep 2012. Madrid. Olivera, C., Redondo, E., Lambert, J., Riera Melis, A., Roca, A., 2006. Els terratrèmols dels segles XIV i XV a Catalunya, Monografie. ed. Institut Cartogràfic de Catalunya, Barcelona.

Olivera, C., Redondo, E., Lambert, J., Riera Melis, A., Roca, A., 2006. Els terratrèmols dels segles XIV i XV a Catalunya. Monografies, 30. Institut Cartogràfic de Catalunya. 407 pp.

Ortuño, M., 2008. Deformación activa en el Pirineo Central: La falla Norte de la Maladeta y otras fallas activas. Universitat de Barcelona, Barcelona, 346 pp.

Ortuño, M., Queralt, P., Martí, A., Ledo, J., Masana, E., Perea, H., Santanach, P., 2008. The North Maladeta Fault (Spanish Central Pyrenees) as the Vielha 1923 earthquake seismic source: Recentactivity revealed by geomorphological and geophysical research. Tectonophysics 453, 246–262. doi:10.1016/j.tecto.2007.06.016

Ortuño, M., Marti, A., Martin-Closas, C., Jimenez-Moreno, G., Martinetto, E., Santanach, P., 2013. Palaeoenvironments of the Late Miocene Pruedo Basin: implications for the uplift of the Central Pyrenees. J. Geol. Soc. London. 170, 79–92. doi:10.1144/jgs2011-121

Palenzuela, J.A., Marsella, M., Nardinocchi, C., Pérez, J.L., Fernández, T., Chacón, J., Irigaray, C., 2015. Landslide detection and inventory by integrating LiDAR data in a GIS environment. Landslides 12, 1035–1050.

Petley, D.N., Dunning, S.A., Rosser, N.J., 2005. The analysis of global landslide risk through the creation of a database of worldwide landslide fatalities, in: Hungr, O, Fell, R., Couture, R., and Ebergardt, E. (Ed.), Landslide Risk Management. A.T. Balkema, pp. 367–374.

Philip, H., Bousquet, J.C., Escuer, J., Fleta, J., Goula, X., Grellet, B., 1992. Présence de failles inverses d'âgequaternairedansl'EstdesPyrénées: implications sismotectoniques. C. R. Acad. Sci. Paris 314, 1239–1245.

Poblet, J., 1991. Estructura herciniana i alpina del vessant sud de la zona axial del Pirineu central. Universitat de Barcelona, 604 pp.

Razak, K.A., 2014. Airborne laser scanning: for forested landslides investigation in temperate and tropical environments. Enschede, The Netherlands. doi:10.3990/1.9789036536257

Roering, J.J., Mackey, B.H., Marshall, J.A., Sweeney, K.E., Deligne, N.I., Booth, A.M., Handwerger, A.L., Cerovski-Darriau, C., 2013. "You are HERE": Connecting the dots with airborne lidar for geomorphic fieldwork. Geomorphology 200, 172–183. doi:10.1016/j.geomorph.2013.04.009

Schmidt, H., 1931. Das Pälazoikum der spanischen Pyrenänen. Abh. Ges. Wiss. Göttingen math,phys. 5, 1–85.

Schulz, W.H., 2004. Landslides mapped using LIDAR imagery, Seattle, Washington.

Serrat, D., Bordonau, J., Furdada, G., Gómez, A., Martí, J., Martí, M., Salvador, F., Ventura, J., Vilaplana, J.M., 1994. Síntesis cartográfica del glaciarismo surpirenaico oriental, in: García-Ruíz, M.B. and (Ed.), El Glaciarismo Surpirenaico: Nuevas Aportaciones. Logroño, Spain, pp. 9–15.

Sibson, R., 1981. A Brief Description of Natural Neighbor Interpolation, in: John Wiley & Sons (Ed.), Interpolating Multivariate Data. John Wiley & Sons, New York, pp. 21–36.

Slatton, K.C., Carter, W.E., Shrestha, R.L., Dietrich, W., 2007. Airborne Laser Swath Mapping: Achieving the resolution and accuracy required for geosurficial research. Geophys. Res. Lett. 34, n/a–n/a. doi:10.1029/2007GL031939

Smith, M.J., Clark, C.D., 2005. Methods for the visualization of digital elevation models for landform mapping. Earth Surf. Process. Landforms 30, 885–900. doi:10.1002/esp.1210

Soeters, R., Rengers, N., 1983. Dos ejemplos de hundimientos gravitacionales en los alrededores de Caldes de Bohi (Pirineos Leridanos), in: Ríos, J.M. (Ed.), Libro Jubilar. IGME, Madrid, Spain, pp. 193–202.

Stange, K.M , Van Balen, R.T., Garcia-Castellanos, D., Cloetingh, S., 2014. Numerical modelling of Quaternary terrace staircase formation in the Ebro foreland basin, southern Pyrenees, NE Iberia. Basin research, 1-23.

Susagna, T., Roca, A., Goula, X., Batllo, J., 1994. Analysis of macroseismic and instrumental data for the study of the 19 November 1923 earthquake in the Aran Valley (Central Pyrenees). Nat. Hazards 10, 7–17.

Tarolli, P., 2014. High-resolution topography for understanding Earth surface processes: Opportunities and challenges. Geomorphology 216, 295–312. doi:10.1016/j.geomorph.2014.03.008

Tarolli, P., Sofia, G., Dalla Fontana, G., 2012. Geomorphic features extraction from high-resolution topography: Landslide crowns and bank erosion. Nat. Hazards 61, 65–83. doi:10.1007/s11069-010-9695-2

Terrasolid, 2015. Terrasolid [WWW Document]. URL http://www.terrasolid.com

Turu, V., Ventura, J., Ros, X., X Pèlachs, A., Vizcaino, A. Soriano, J.M. 2011. Geomorfologia glacial del tram final de la Noguera Pallaresa i riu Flamicell (els Pallars). Extended abstracts of the XIII Reunión Nacional de Cuaternario: El Cuaternario en España y áreas afines, avances en 2011. Andorra.37-43.

Van Den Eeckhaut, M., Poesen, J., Verstraeten, G., Vanacker, V., Nyssen, J., Moeyersons, J., Beek, L.P.H. van, Vandekerckhove, L., 2007. Use of LIDAR-derived images for mapping old landslides under forest. Earth Surf. Process. Landforms 32, 754–769. doi:10.1002/esp.1417

Van Den Eeckhaut, M., Poesen, J., Gullentops, F., Vandekerckhove, L., Hervás, J., 2011. Regional mapping and characterisation of old landslides in hilly regions using LiDAR-based imagery in Southern Flanders. Quat. Res. 75, 721–733. doi:10.1016/j.yqres.2011.02.006

Van Den Eeckhaut, M., Hervás, J., 2012. State of the art of national landslide databases in Europe and their potential for assessing landslide susceptibility, hazard and risk. Geomorphology 139-140, 545–558. doi:10.1016/j.geomorph.2011.12.006

Van Den Eeckhaut, M., Kerle, N., Poesen, J., Hervás, J., 2012. Object-oriented identification of forested landslides with derivatives of single pulse LiDAR data. Geomorphology 173-174, 30–42. doi:10.1016/j.geomorph.2012.05.024

Varnes, D.J., 1978. Slope movements. Types and processes. En: Schuster & Krizker (Eds), "Landslides: analysis and control". Transportation Research Board, National Academyof Sciences, vol. 176. Special Report, Washington D.C., 11-35.Vilaplana, J.M., 1983. Quaternary Glacial Geology of Alta Ribagorça Basin (Central Southern Pyrenees). Acta Geologica Hispanica, 18, (314), 217-233. http://www.raco.cat/index.php/ActaGeologica/article/viewFile/75140/97983

Zandvliet, J., 1960. Geology of Upper Salat and Pallaresa Valleys, Central Pyrenees, France-Spain. Leidse Geol Meded 25, 1–127.

Zarroca, M., Linares, R., Roqué, C., Rosell, J., Gutiérrez, F., 2014. Integrated geophysical and morphostratigraphic approach to investigate a coseismic (?) translational slide responsible for the destruction of the Montclús village (Spanish Pyrenees). Landslides 11, 655–671. doi:10.1007/s10346-013-0427-z

Zischinsky, U., 1966. On the deformation of high slopes, in: Proceedings, 1st Congress of the International Society of Rock Mechanics. International Society of Rock Mechanics, pp. 179–185.

FIGURE CAPTIONS

Fig. 1. Study area location and geological and geomorphological context. **A**) Location of the study area within the Pyrenees; **B**) Area surrounding the study area with the closest active faults, taken from Lacan and Ortuño (2012), and the location of the epicenters of the 1923 Vielha earthquake (M_L = 5.2; Susagna et al., 1994) and the 1373 Ribagorça earthquake ($M_W \approx 6.2$; Poblet, 1991; Olivera et al., 2006). The inferred faults have been studied by Briais et al. (1990), Philip et al. (1992), Calvet (1999), Carozza and Baize (2004), Ortuño (2008), and Ortuño et al. (2008, 2013) among others. **C**) Main geological units. Thrust faults are symbolized by lines with triangular teeth and normal faults with solid lines. Hillshade map used as background has a sun azimuth 315º and sun altitude 45º. Coordinate system used is ETRS 89, zone 31N. Black squares frame the study area showed in Figs. 2 and 3.

Fig. 2. Map of the main geomorphological features of the study area with main geomorphological features, rivers and major streams. Aerial orthophoto with 25 cm resolution from the ICGC is used as background.

Fig. 3. Geomorphological features detected on the studied zone in relation to slope failures. The limits of the areas studied are indicated. Hillshade map with sun azimuth 315º and sun altitude 45º is used as background.

Fig. 4. Features detected in Zone A and comparison of the visibility of these features in different base layers. (**A**) Aerial orthophoto with 25 cm resolution from the ICGC; (**B**) 5 m DEM without interpretation; (**C**) 1 m DEM without scarps; (**D**) 1 m DEM with scarps and main failure features.

Fig. 5. Features detected in Zone B and comparison of the visibility of these features in different base layers. (**A**) Aerial orthophoto with 25 cm resolution from the ICGC; (**B**) 5 m DEM without interpretation; (**C**) 1 m DEM without interpretation; (**D**) 1 m DEM with scarps and main failure features. Note that the hypothetic location of the ancient

portion of the Portainé glacial cirque affected by a landslide is indicated with a dashed line.

Fig. 6. Features detected in Zone C and comparison of the visibility of these features in different base layers. (**A**) Aerial orthophoto with 25 cm resolution from the ICGC; (**B**) 5 m DEM without interpretation; (**C**) 1 m DEM without interpretation; (**D**) 1 m DEM with scarps and main failure features.

Fig. 7. Examples of the hillshade maps generated from the LiDAR data by using different azimuths in the illumination angle for zones A1 and A3 (see Fig. 3 for their location). All of the examples have a sun altitude of 45º. Note how scarps oriented NE-SW are highlighted with sun at 315º and 135º, but hidden at 45º and 225º. The most complete view of the three semicircular scarps located at the W of this figure, in Zone A3, is given by the 315º hillshade map. The thorough identification of the maximum number of scarps was only possible with the 3D view in Fig. 8.

Fig. 8. 3D view of the hillshade (sun azimuth 315º and sun altitude 45º) on a portion of the studied zone. In the upper image, only the boundaries of the zones A and B are included. In the lower image, the geomorphological features mapped are shown.

Fig. 9. Example of some features in zone A1 observed in the field. Map with the locations of the scarps is also shown. (1) Scarp #1: 2 m high in the observation point but 4 m in maximum height. (2) Scarp #2: 2.5 m high. (3) Portion of the lowest and sharpest part of the head scarp #3: 2 m high, but the highest parts of this scarp being 15 m high. (4) Scarp #4: 4 m high at the observation point but 15 m in maximum height. (5) Scarp #5: 0.5 m in maximum height.

Fig. 10. Example of some features in zone B observed in the field. Map with the location of the features is also shown. (1) Scarp #1: 1 m high in the observation point. (2) Scarp #2: Secondary scarp affecting the Portainé cirque and 3 m high at the observation point. (3) Cracks observed between the southern cirques with a maximum height of 1.2 m. (4) Scarp #4: It corresponds to the slope failure affecting the Portainé cirque with a maximum height of 15 m. (5) Antislope scarp #5: 1.5 m in maximum height. (6) View of zone B1 showing how the forest hinders the identification of failure features in this zone.

Fig. 11. Topographic profiles along different slopes affected by failures. See Fig. 3 for location of the sections. The main scarps identified are continued under the slope according to surfaces calculated from the 3D lines mapped using the 1 m DEM. The most likely mobilized mass is marked in grey.

TABLES

Table 1. Range of flight and system parameters corresponding to the different strips covering the Portainé study zone.

Table 2. Summary table with the geometrical characteristics (maximum, max, and minimum, min, values) of the slope failures identified in the Portainé zone and their perceptibility within the aerial photos, the orthophotos and in the 5 m DEM. The maximum dip of the slope where the failures are located is included only for the cases with relatively constant slopes.

Table 3. Summary of the slope failures clustering near the Noguera Pallaresa valley (next to the Portainé study area). All of them are located within 10 km around the Rialp village. Some of them are published, some of them in the LLISCAT Data Base [on line] (see references), and some of them are known by the authors of the present work but not published (reported in the table as 'com. pers.').

Figure 1

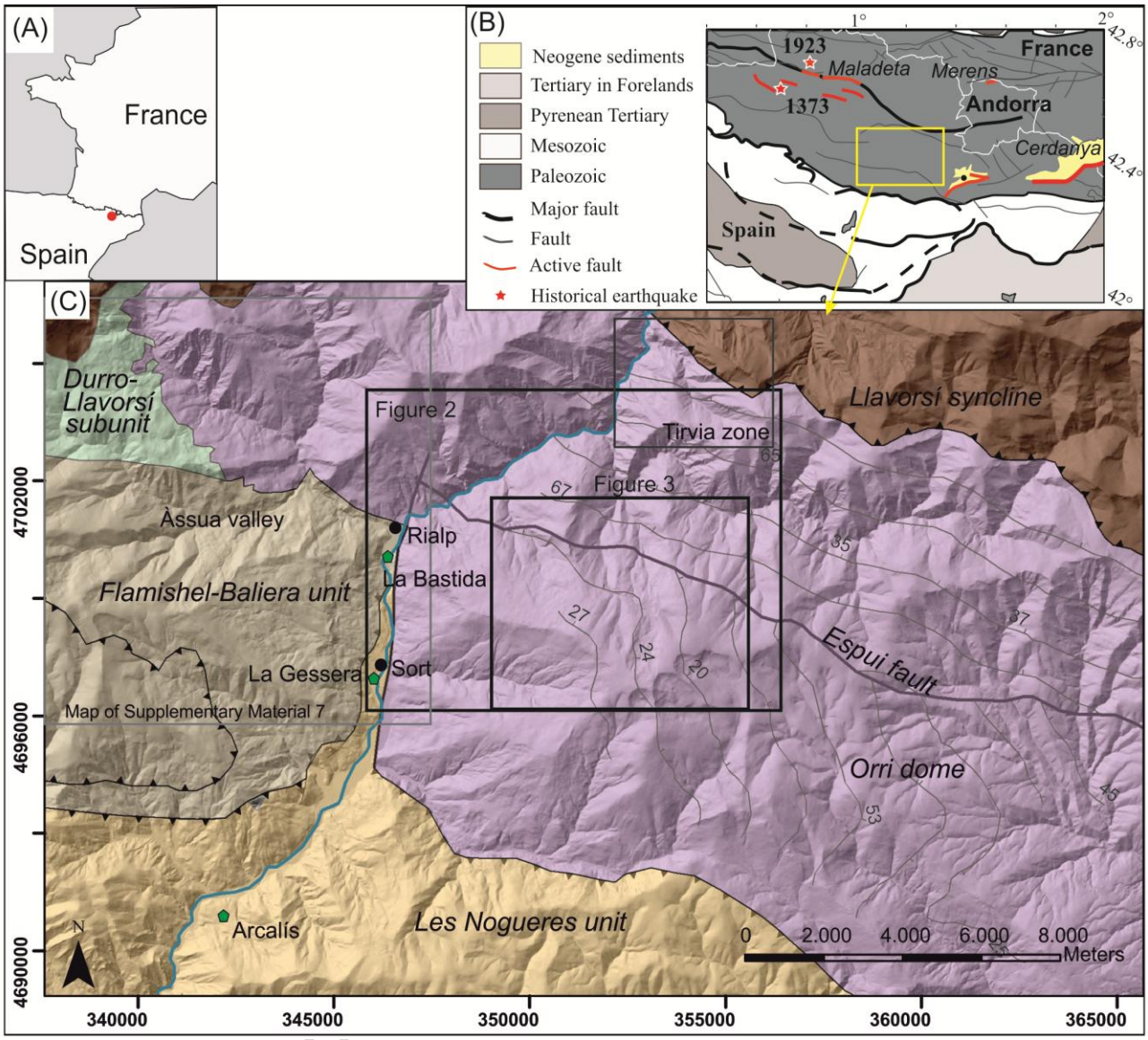

Figure 2

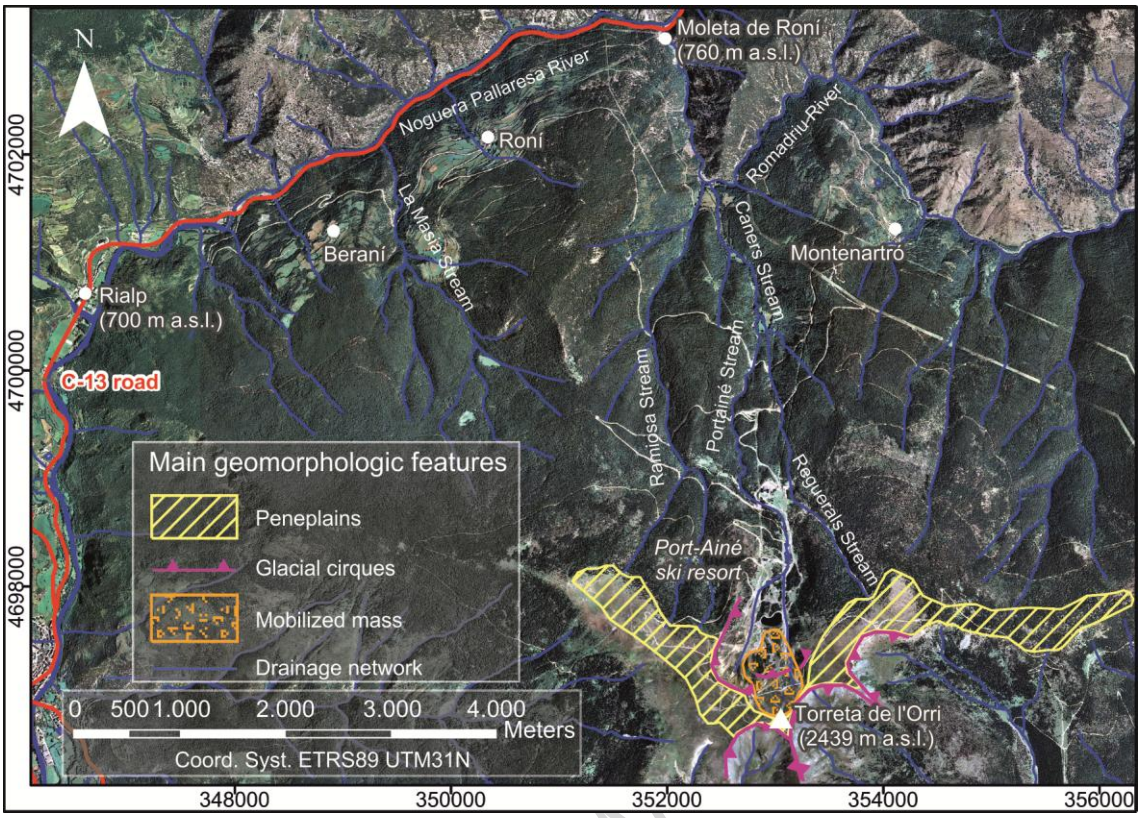

Figure 3

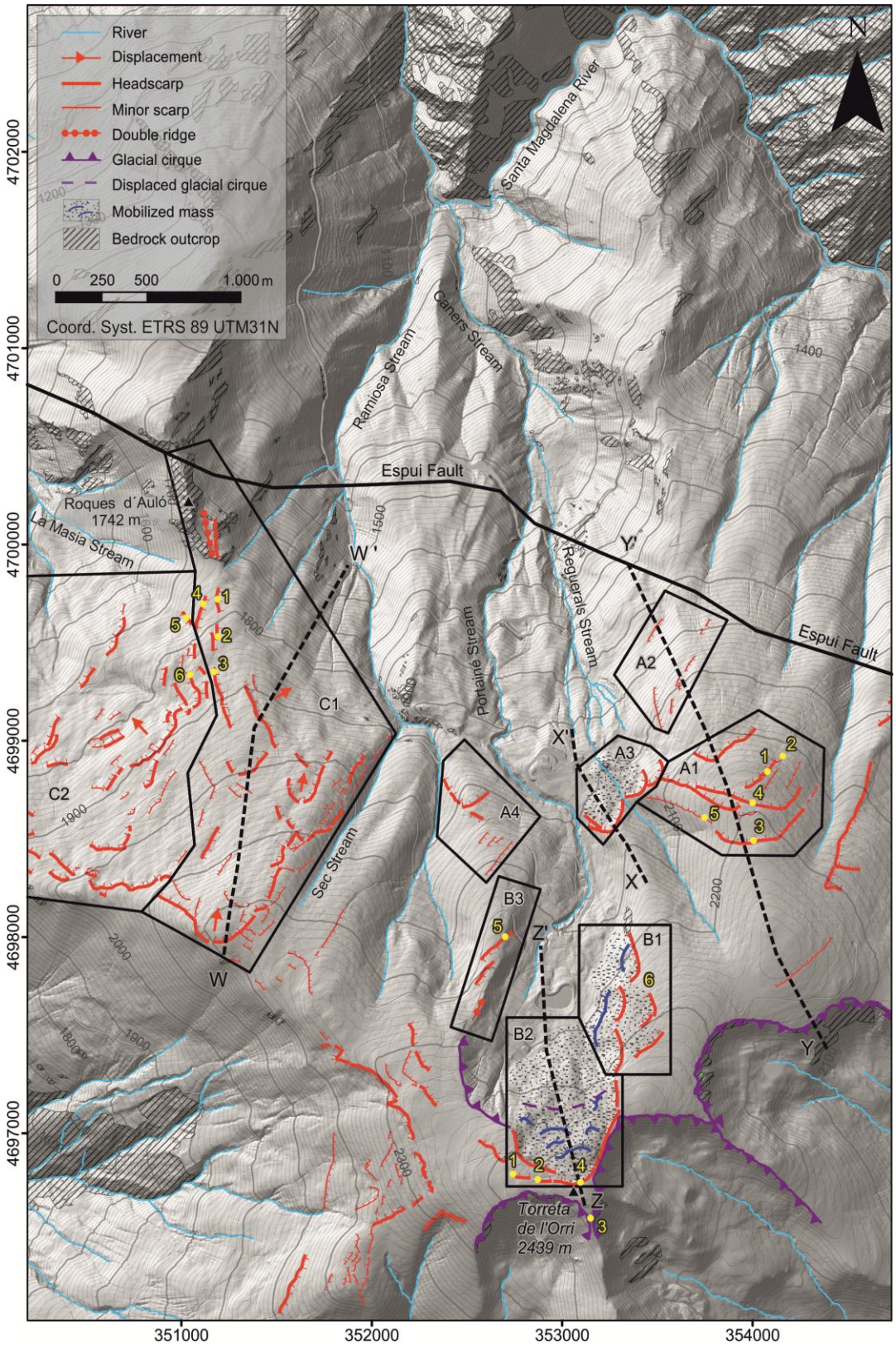

Figure 4

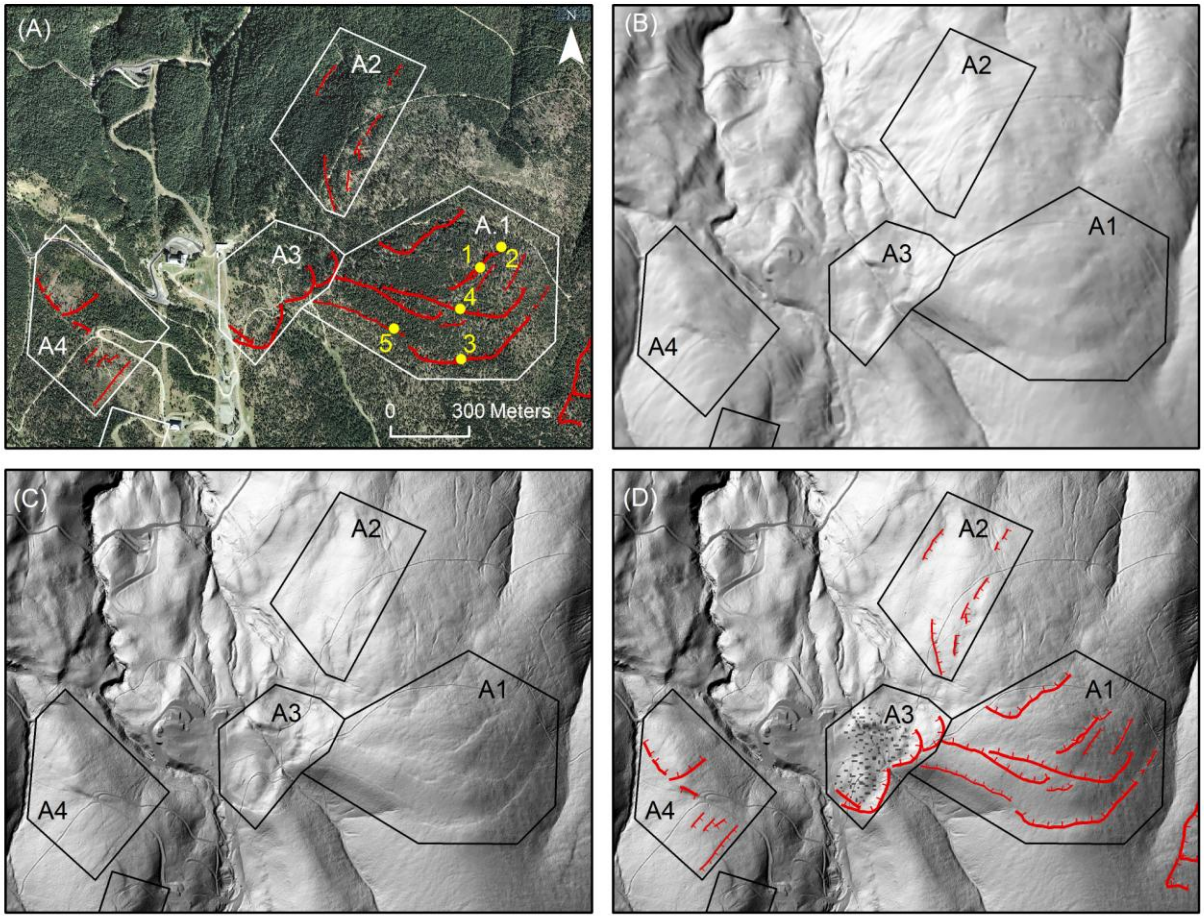

Figure 5

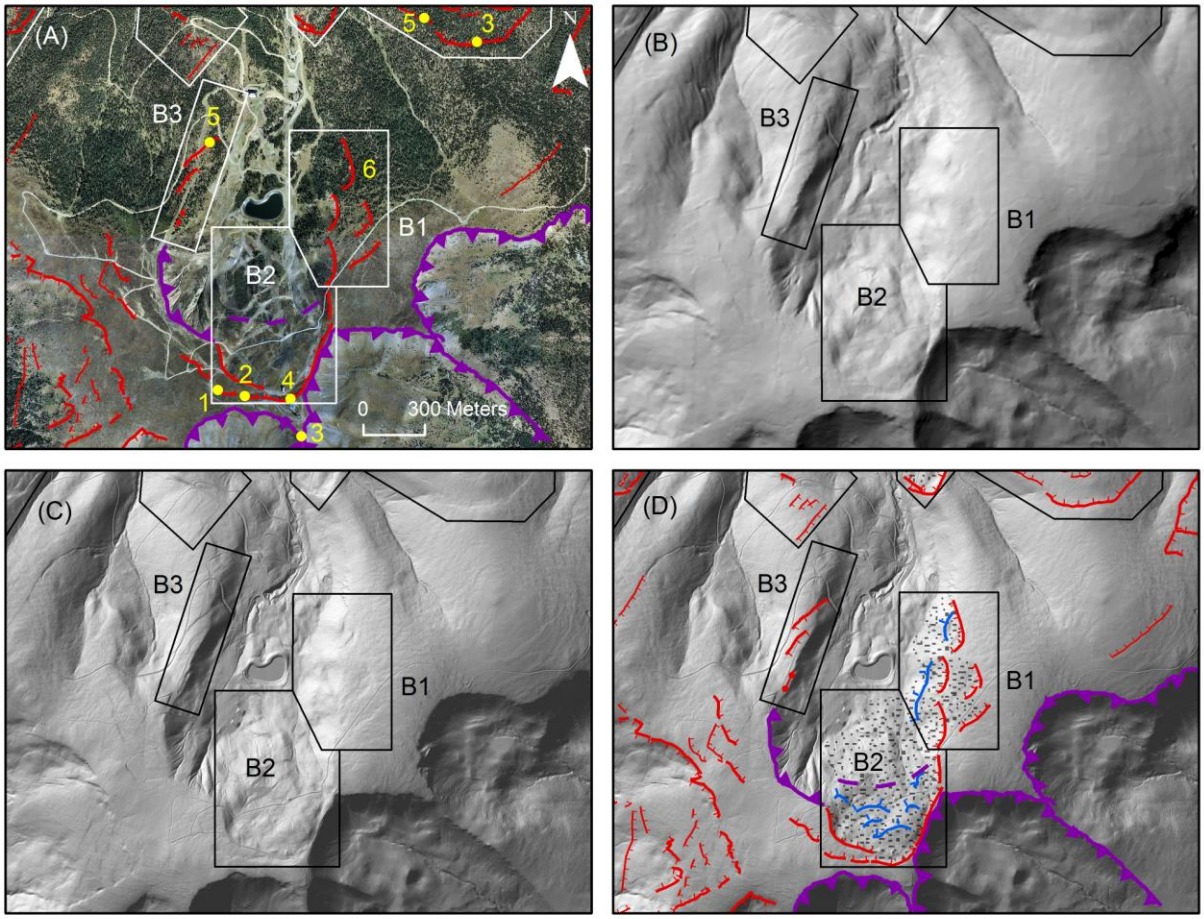

Figure 6

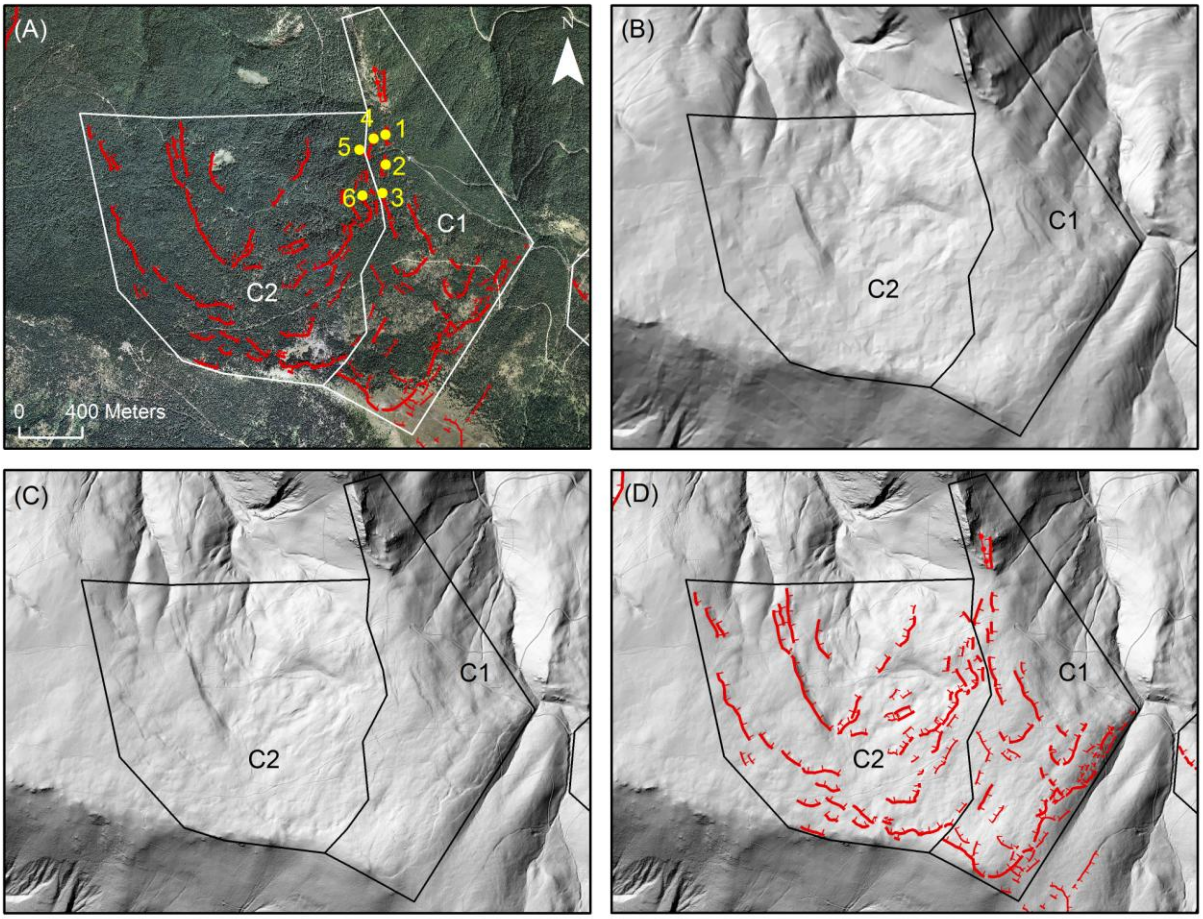

Figure 7

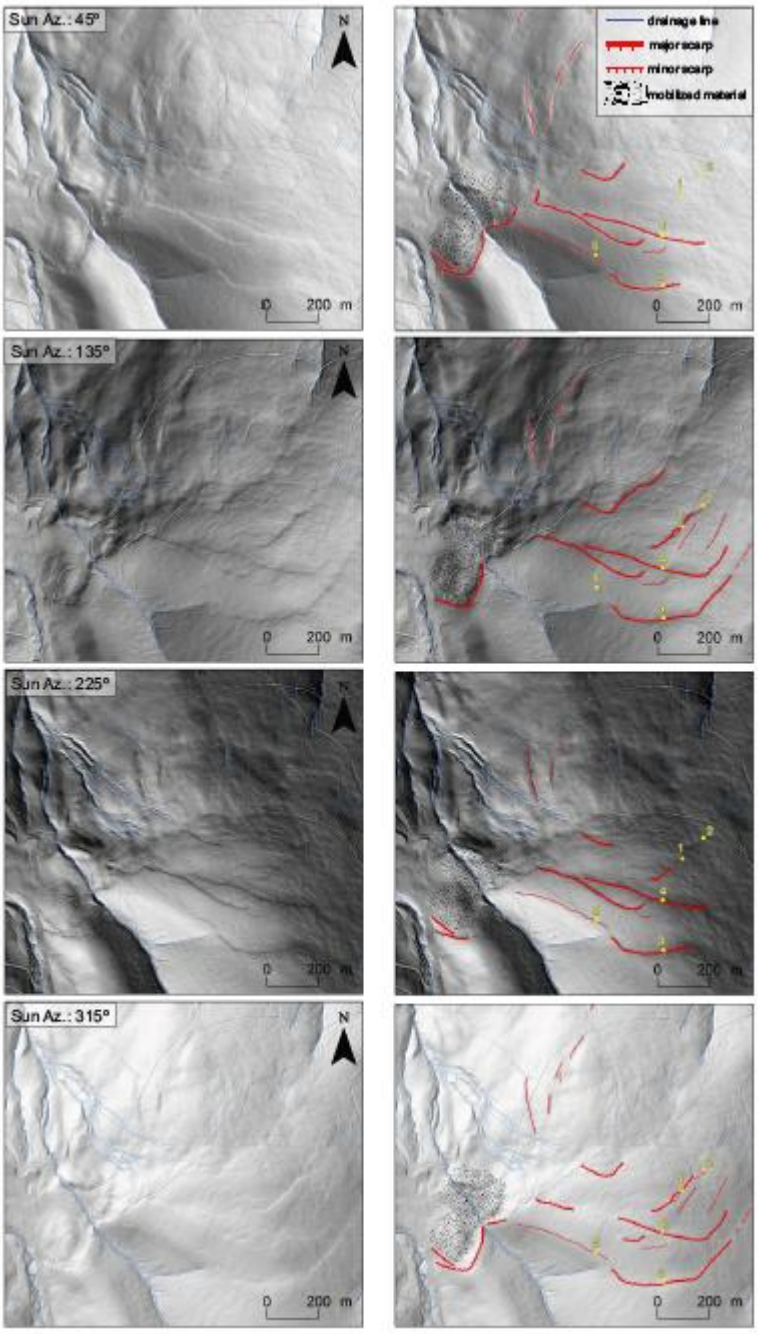

Figure 8

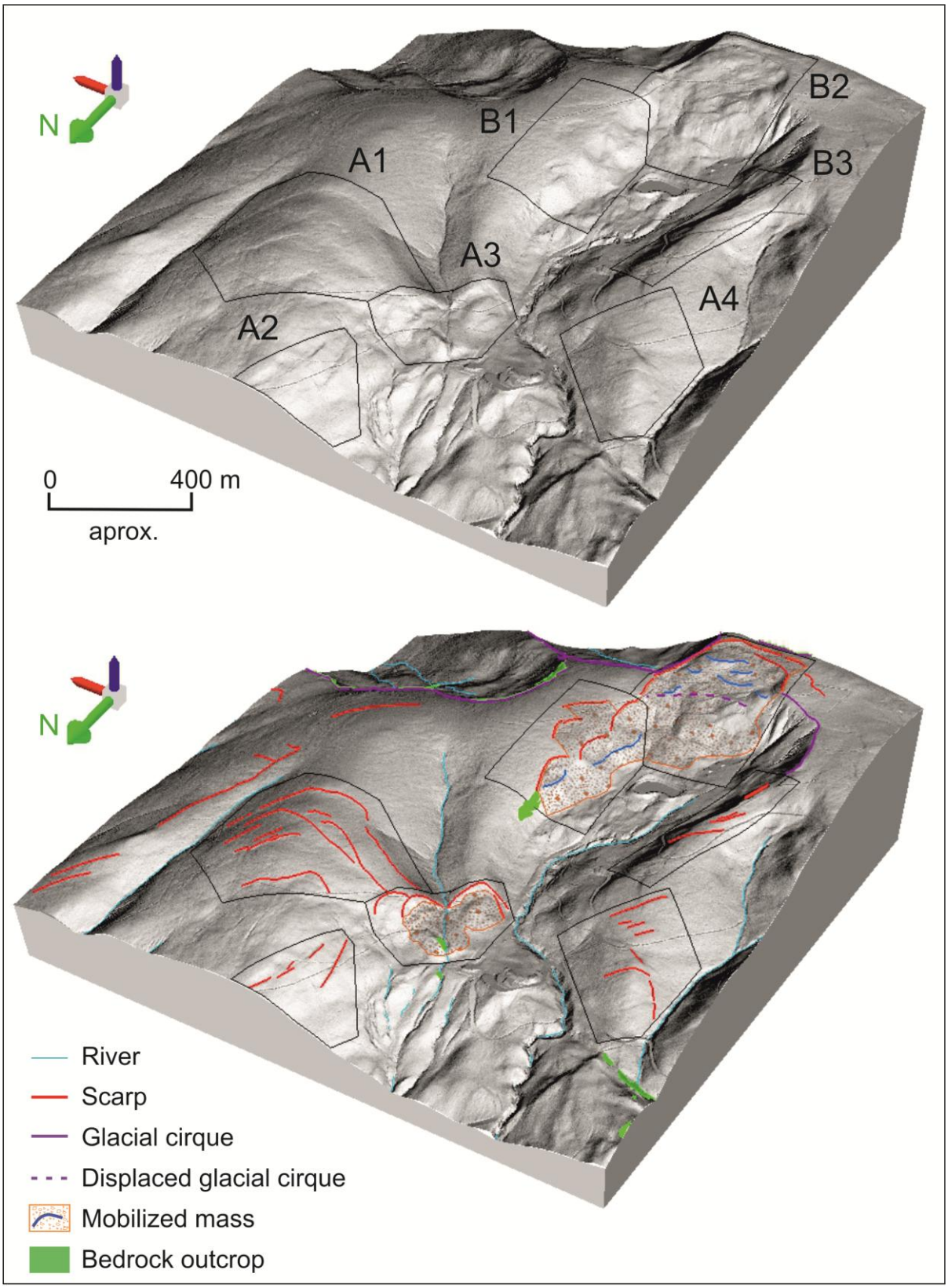

Figure 9

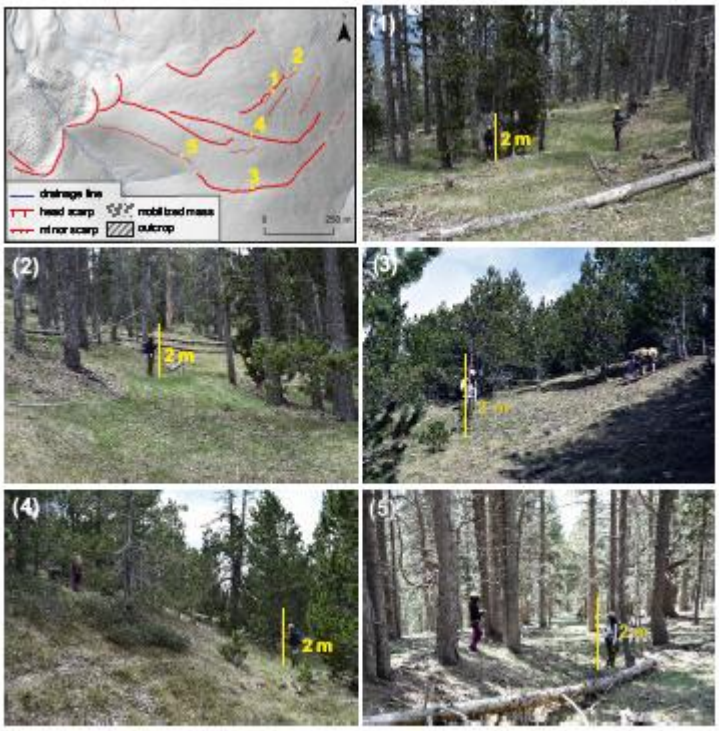

Figure 10

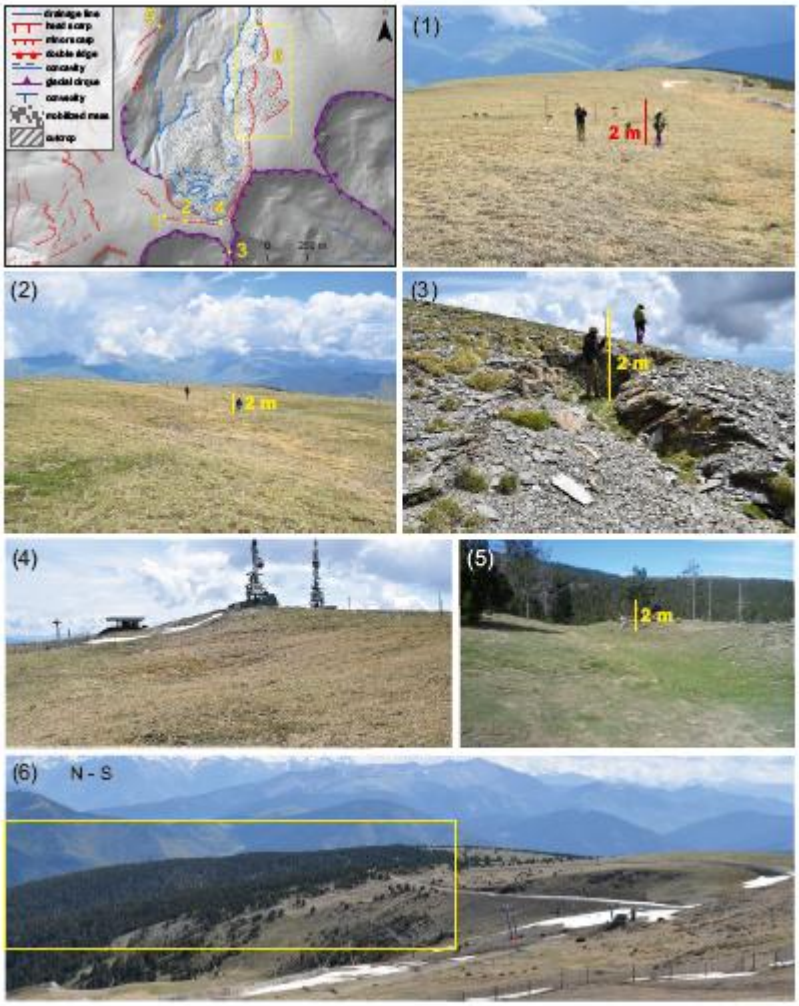

Figure 11

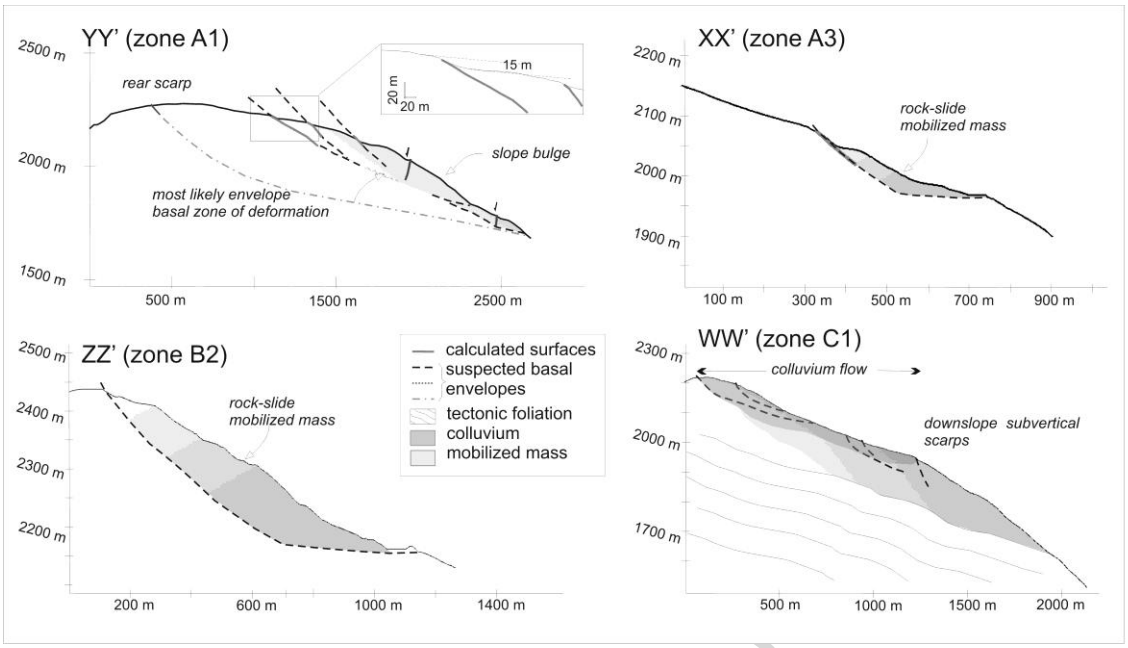

Table 1. Range of flight and system parameters corresponding to the different strips

Date	July–August 2009 and August–September 2011
# strips + cross strips	35 + 2
Flying speed (knots)	100–165
Flying altitude (m a.g.l.)	2113–2440
Laser repetition rate (Hz)	84400–96100
Scan frequency (Hz)	21.5–32
Scan width (FOV)	37°–48°
Swath width (m)	1620–2098
Footprint size (m)	0.48–0.59
Point density (points m^{-2})	0.8–2.86
Vertical precision (cm)	11–14
Horizontal precision (cm)	28–32

Table 2. Summary table with the geometric characteristics of the landslides identified in the Portainé zone and their perceptibility within the aerial photos, the aerial orthophotos and in the 5 m DEM. The maximum dip of the slope where the failures are detected is included for the cases where the slope is relatively constant.

Zone (name)	**Type**	**Length (*L*) and height (*H*) of the scarps (max/min)**	**Slope Dip (º)**	**Visible in the Aerial photos/ Orthophotos (Y, yes/N, not)**	**Visible in the 5-m topography (Y, yes/N, not)**	**Area (km^2)**
Zone A						
A1 +A2	Slope deformation	*L* (1000/100 m) *H* (15 /0.3 m)	<10(A.1) 10–17 (A.2)	N (only major head-scarp in A1)	N	0.55
A3	Arrested RSF	*L* (312 m) *H* (25 /10 m)	22–26	N	Y	0.11
A4	Slope deformation	*L* (223 / 60 m) *H* (3.5/0.5 m)	12-18 (upper) ~20 (lower)	Y (in the orthophoto and non-forested area)	N	0.14
Zone B						
B1 + B2	Arrested RSF	*L* (900/86 m) *H* (15/1 m)		Y (although minor rear-scarps in zone B2 are not detected)	Y	0.70
B3		*L* (300/60 m) *H* (25/1 m)		Y	Y	0.12
Zone C						
C1	Complex colluvium flow and RSF	*L* (1043/80 m) *H* (4/2.5 m)	10–15 (C1.a) 25-30(C1.b)	N (only the upper head- scarp and double ridge)	N	1.43
C2	Superficial SF	*L* (280/30 m) *H* (5/0.5 m)	15–25	N	N	2.50

Table 3. Summary of the slope failures clustering along the Noguera Pallaresa valley next to the Portainé study area. All of them are located within 10 km around Rialp Village (Fig. 1). Some of them are included in published papers and in an MSc thesis, some of them in the Lliscat Data Base [on line] (see references), and some of them have been identified by the authors of the present work but are not published (reported in the table as 'pers. comm.').

Location	Slope failure number	Closest village	Km and direction from Rialp	Reference
Vall d'Àssua	>20	Rialp – Sort (W and S)	0–4 (South)	Furdada and Vilaplana (1988); 9 in Lliscat [on line]
Barranc de Montardit	>5	Montardit (W)	8 (South)	Furdada and Guinau, pers. comm.
Malmercat	1	Montardit (SE)	8 (South)	Lliscat [on line]
Barranc d'Escós	>5	Baro (W)	12 (South)	Furdada, com. pers.; 1 in Lliscat [on line]
Arcalís	1	Baro (SE)	12 (South)	Furdada, pers. comm.
Llagunes	1	Sort (E)	17 (South-East)	Furdada, pers. comm.
Barranc de Boés	1	Llavorsí (NW)	10 (North-East)	Corominas et al. (2004). Lliscat [on line]
Tirvia	At least 6	Tirvia	12–15 (North-East)	Nàquira (2016)

Graphical abstract

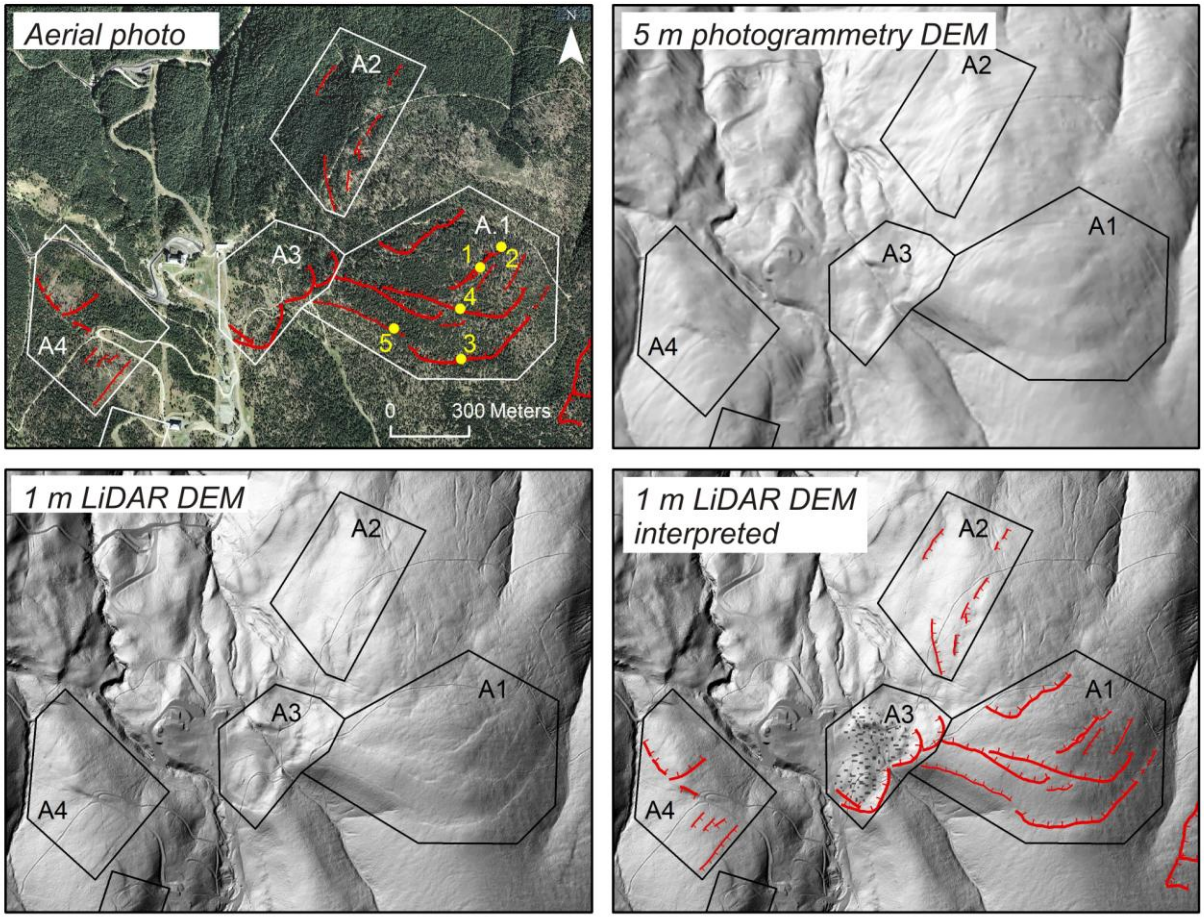

Highlights

Near 120 scarps, many of them less than 1 m high and located under the forest, were identified through analysis of LiDAR derived DEMs

- The geomorphological analysis of LiDAR data emerges as a powerful tool to map subtle landforms of incipient slope failures, enabling to improve the completeness of geomorphological landslide inventories.
- Three areas affected by Rock Slope Failures and one Superficial Failure were recognized for the first time within the mountainous area of Portainé (Central Pyrenees)